Applied Surface Science 610 (2023) 155530

Contents lists available at ScienceDirect

Applied Surface Science

journal homepage: www.elsevier.com/locate/apsusc

Full length article

# Temperature-modulated synthesis of vertically oriented atomic bilayer graphene nanowalls grown on stainless steel by inductively coupled plasma chemical vapour deposition

Enric Bertran-Serra [a,b,*], Arevik Musheghyan-Avetisyan [a], Stefanos Chaitoglou [a,b], Roger Amade-Rovira [a,b], Islam Alshaikh [a,b], Fernando Pantoja-Suárez [a,c], José-Luis Andújar-Bella [a,b], Tariq Jawhari [d], Angel Perez-del-Pino [e], Enikö Gyorgy [e]

[a] ENPHOCAMAT (FEMAN) Group, Department of Applied Physics, Universitat de Barcelona, Martí i Franquès 1, E-08028 Barcelona, Spain
[b] Institute of Nanoscience and Nanotechnology (IN2UB), Universitat de Barcelona, E-08028 Barcelona, Spain
[c] Departmento de Materiales, Facultad de Ingeniería Mecánica, Escuela Politécnica Nacional, Ladrón de Guevara, E11-253 Quito, Ecuador
[d] CCiT, Universitat de Barcelona, Lluís Solé i Sabaris, 1-3, E-08028 Barcelona, Spain
[e] Institute of Materials Science of Barcelona (ICMAB), CSIC, Campus UAB, E-08193 Bellaterra, Spain

ARTICLE INFO

*Keywords:*
Graphene nanowalls
VGNW
Bilayer graphene
Stainless-steel substrate
ICP-CVD
Raman analysis
Flexible electrodes

ABSTRACT

It is now clear that growing flat graphene nanostructures from the gas phase on planar substrates is possible. One of the keys to success —particularly in producing a very large specific surface in a reduced space— is the use of 3D carbon nanostructures (i.e., vertical graphene nanowalls, VGNWs) over a planar substrate as a growth template for the deposition of electrochemically active materials (as, for example, transition metal oxides (TMO)). Vertical graphene nanowalls, also known as petal-like, vertical graphene flakes or vertical graphene, can achieve a very large specific surface area of 1100 $m^2/g$, which is comparable to or greater than that of carbon nanotubes —the reference material for its use in high-performance supercapacitors or in other energy-related applications requiring a large active surface area. Vertical graphene nanowalls also exhibit high vertical and in-plane electrical conductivity when grown on metal electrodes, which benefits their use in electrochemical applications. Here, we focus on the growth of VGNWs on flexible stainless-steel substrates (SS310), in principle suitable for applications to electrodes of electrochemical systems (batteries, supercapacitors, catalysts), by inductively coupled plasma chemical vapour deposition (ICP-CVD), from methane as a carbon precursor, in a wide range of temperatures (575 to 900 °C). We will discuss the effect of growth temperature on morphological and structural characteristics of VGNWs based on the results of Raman spectroscopy and field emission scanning electron microscopy (FE-SEM) analysis. Because the nanostructures of graphene nanowalls reported to date are, for the most part, based on multi-layered graphene, here we seek to highlight the effect of temperature on the number of atomic layers of VGNW. In the 700–750 °C range, and under the plasma conditions explored, vertical graphene nanowalls are bilayer, which is foreseen to directly affect the magnitude of the VGNW specific surface.

## 1. Introduction

It has been 20 years since two-dimensional (2D) graphene began to be studied and exploited for many applications [1,2]. Originally, two-dimensional graphene was obtained by exfoliating layers of crystalline graphite (usually from high oriented pyrolytic graphite, HOPG). However, the morphology and characteristics required for certain applications was somewhat limited if we compare this top-down synthesis method with the bottom-up methods that have later been proposed. This is the case of graphene produced from the vapour phase. It is now widely recognized that it is possible to grow planar graphene nanostructures from the gas phase on flat substrates [3], but for applications where very large areas are required in a small space, the use of three-dimensional (3D) graphene nanostructures is a much more suitable option. Specifically, we refer to vertical graphene nanowalls (VGNWs) on a flat substrate, initially known as graphite petal-like [4] and also called vertical

* Corresponding author at: ENPHOCAMAT (FEMAN) Group, Department of Applied Physics, Universitat de Barcelona, Martí i Franquès 1, E-08028 Barcelona, Spain.
*E-mail address:* ebertran@ub.edu (E. Bertran-Serra).

https://doi.org/10.1016/j.apsusc.2022.155530
Received 6 September 2022; Received in revised form 20 October 2022; Accepted 28 October 2022
Available online 3 November 2022
0169-4332/© 2022 UNIVERSITAT DE BARCELONA. Published by Elsevier B.V. This is an open access article under the CC BY license (http://creativecommons.org/licenses/by/4.0/).

graphene flakes or vertical graphene, which can act as a growth support for the deposition of nanostructures of electrochemically active materials (such as transition metal oxides, TMO). These hybrid structures provide a very effective solution to the need for chemically stable electrodes, with high electrical conductivity and very high specific surface area [5]. In the case of VGNWs grown on metallic substrates, this conductivity is manifested in three dimensions, which is of interest in electrochemical energy storage and catalysis applications [6] due to the very large active specific surface associated with these nanostructures. VGNWs can achieve a very large specific surface area of 1100 $m^2/g$ [7], a value comparable to or greater than that of carbon nanotubes, which is a reference material for its use in energy-related applications requiring a large active surface.

Applications of VGNW's on electrodes span multiple fields, such as energy storage (fuel cells, supercapacitors, and batteries) [8–10], gas sensors [11], flexible electrodes [12], communication and imaging (ultra-fast terahertz technology and field emission) [13,14], among others.

In this study, we focus on the growth of VGNWs on flexible stainless steel substrates, SAE 310 (SS310), which is in principle suitable for applications to electrodes of electrochemical systems (batteries, supercapacitors, catalysts) [15–18]. Specifically, we seek to study the effect of growth temperature on the morphological and structural features of VGNWs.

Thanks to its chemical stability and high electrical conductivity, stainless steel (SS) is widely used as an electrode in electrochemical systems [19]. However, the growth of carbon nanostructures on stainless steel at high temperatures is a complex process, since the composition of stainless steel (mainly based on Fe, Cr, and Ni) on the substrate's surface can vary considerably. The substrate's surface state affects the nucleation process directly and, subsequently, the growth of carbon nanostructures: the diffusion and solubility of carbon in the Fe—Cr phase can increase significantly with the growth temperature and, as we will see later, can drastically affect the growth of carbon nanostructures.

Various research groups have studied the growth of graphene nanowalls on stainless steel sheets [20,21] and on silicon, silicon oxide and silicon/metal substrates [22–24], focusing on various aspects such as low growth temperature ($< 500\ ^\circ C$), and bias voltage [21], and others on chemical properties and morphological characteristics for applications to energy, catalysis and sensors. However, there is still little experimental evidence to bring to light the complex growth phenomena that take place during the growth of graphene nanowalls. In the present work, we carry out a detailed study of the effect of growth temperature on the structural quality and microscopic characteristics of VGNW grown on stainless steel. Our results show that the synthesis of VGMWs is improved by applying the most suitable temperature, which keeps defects at a minimum while still providing atomic bi-layer thickness. Based on the applications mentioned above, having a high specific surface area of high-quality vertical graphene with great chemical stability is in many ways advantageous. On the other hand, while having a high number of defects in the VGNWs might in some instances seem convenient, not all defects are the same and they do not even act in the same way. Our Raman spectroscopy data show that there are two types of defects, the most convenient ones being those located at the sharp edges of the VGNWs [24], which do not detract from the quality of the graphene structures, in applications such as electrodes in supercapacitors or in electrocatalysis. Sharp edge sites exhibit higher charge density than internal carbon atoms of the nanostructure, thus promoting the process of proton adsorption and reduction [25,26].

As proof-of-principle, we present the analysis of the results obtained from the Raman spectra and field emission scanning electronic microscopy (FE-SEM) of VGNWs grown on flexible substrates of SS310. These were obtained by means of a pure methane plasma in a wide range of temperatures (575 to 900 °C), using an inductively coupled plasma chemical vapour deposition (ICP-CVD) reactor, described elsewhere [27]. Although, as reported in the literature, these nanostructures are generally based on few-layer and multilayer graphene [28], and have a large specific surface area, here we show evidence of the effect of temperature on the number of atomic layers of VGNWs/SS310 samples. Thus, in the growth temperature range of 700–750 °C, under the plasma conditions explored in our study, the vertical graphene nanowalls grow in the form of a bilayer, which significantly increases their specific surface area.

Importantly, our study of synthesis of graphene nanowalls in a wide range of growth temperatures is the first one carried out by ICP-CVD in which an optimal temperature for the production of bilayer graphene nanowalls suitable for energy storage applications is established.

## 2. Experimental details

Carbon nanostructures were grown in an ICP-CVD reactor, which was modified and improved from a previous one described elsewhere [27]. The new system was configured to work at 13.56 MHz at an RF power of 400 W using a thermostatic tubular oven and a pressure control system. It consists of a long quartz tube (150 cm long, and 6 cm of diameter) having an RF anti-resonator coil manufactured by winding a copper tube with a diameter of 6 mm and a length of a quarter of the wavelength (552.7 cm) of the RF signal (13.56 MHz) on a cylinder with a diameter of 10 cm and a length of 23 cm. The resulting coil was shielded by an outer metal cylinder, with a diameter of 15 cm and a length of 25 cm, connected to ground. In order to obtain a standing wave under resonant/anti-resonance conditions, one end of the coil was connected to ground and the other end was kept at open circuit, respectively. The connection to the power supply (COAXIAL POWER SYSTEMS, RF generator 1 kW @ 13.56 MHz) was placed midway between the ends of the winding by means of an N-type coaxial cable of 50 Ω of characteristic impedance. The impedance matching was carried out by means of an automatic matching network (AMN1k-13 of COAXIAL POWER SYSTEMS) connected between the source and the anti-resonant coil. The antenna coupled to the quartz tube reactor produces a remote plasma created 40 cm away from the samples. The samples are placed inside the quartz tube, which axially traverses the 35 cm long tubular furnace that can work up to a little over 1000 °C.

Carbon nanostructures were grown on SS310 substrate foils. SS310 is chemically more stable against oxygen and chemicals than other metals such as Cu for use as an electrode. We chose SS310 for its characteristics, such as metallic conductivity, chemical stability, resistance to high temperatures, high Cr content that reduces carbon nucleation from Fe nanoparticles secreted from the substrate [29], carbon compatibility, inertness, and possibility of achieving it as thin elastic sheets (100 μm thick).

For the determination of the mass growth rate, SS310 substrates of equal dimensions (50 mm long, 38 mm width, and 100 μm thick) were used in order to measure the deposited mass of carbon. The values obtained in a multitude of samples varied between 2 and 5 mg for deposition times of 30 min.

Prior to the growth of carbon nanostructures, the quartz tube was thoroughly cleaned, in order to remove possible carbon impurities deposited on its internal surface during previous growth process. To this aim, a small gaseous flow of oxygen (99.99%) was introduced at a pressure of 50 Pa, which when excited by a 400 W RF plasma for about 30 min at room temperature, completely oxidizes the deposited carbon species on the inner surface of the quartz tube. Once the tube is totally transparent, the sample can be introduced into the reactor mounted on its graphite holder. SS310 substrates are routinely cleaned with isopropanol in a 20 min ultrasonic bath. Then, the substrates are weighed using a precision 100 μg balance and introduced mounted on the graphite substrate holder inside the quartz tube. The flat SS310 substrate on the graphite substrate holder is positioned parallel to the quartz tube and 15 mm from its central axis. The substrate remains oriented at a small angle of 5° with respect to the horizontal axis of the tube and

against the incident gas flow. The position of the substrate corresponds to the centre of the tubular oven, 40 cm from the radio frequency antenna. The quartz tube is evacuated by means of a 65 l/s turbo-molecular pump to an ultimate pressure, usually between $10^{-3}$ and $10^{-4}$ Pa. A small flow of $H_2$ (10 sccm) is introduced at a pressure of 1 Pa and the oven heated by a ramp temperature of 1 °C/s to the desired temperature (in the present study, between 575 and 900 °C). Once the temperature of the sample has stabilized, the $H_2$ pressure in the quartz tube is increased to 50 Pa by throttling the conductance valve closing the inlet of the turbo-molecular pump, and a 400 W RF plasma is turned on for 30 s. This operation enables the surface of the SS310 substrate to be activated by reducing the surface oxide. Subsequently, and without delay, a flow of 10 sccm of high purity 53.3 ± 0.5 Pa $CH_4$ (99.995%) is introduced and the hydrogen flow is cut off. At that moment, the growth of carbon nanostructures begins. The pressure was measured by a calibrated absolute pressure meter working in the range of 0 to 2 Torr and it was maintained stable during the experiments by an automatic pressure controller. The RF power supply provided 400 ± 4 W at a frequency of 13.56 MHz, with zero reflected power, all monitored by an external RF power meter. The $CH_4$ mass flow was fixed to 13 ± 1 sccm, and the processing time was 1800 s in all the experiments. These conditions (temperature, gas flow, pressure and RF-power) were maintained constant in all the growing processes. Then, the plasma is turned off, the gas flow is cut off and the temperature is reduced to values close to room temperature within a 15 min interval while the reactor is evacuated to the ultimate pressure. Once the sample has cooled, it can be extracted from the quartz tube.

The composition of the plasma during the growth of VGNWs was investigated by optical emission spectroscopy (OES) using an optical fiber coupled spectrometer (BLACK-Comet® UV-VIS) and collecting optics. The UV-VIS spectrometer is powered directly from a PC's USB port. A single strand optical fiber cable assembly delivers input via standard SMA 905 optical fiber. Each emission spectrum was recorded in a time-integrated manner by using SpectraWiz® software.

In order to study the structure and morphology of the grown VGNWs, a field emission scanning electron microscope (FE-SEM) JEOL JSM-7001F, operated at 20 kV, and a transmission electron microscope (TEM) JEOL 1010, operated at 200 kV were used. The carbon structures were transferred to the TEM grid by simply scratching off from the substrates.

Ternary phase diagrams of the SS310 substrate were plotted using THERMO-CALC® software. The concentration of Cr, Ni and Fe of the samples grown at different temperatures were obtained by energy-dispersive X-ray spectroscopy (EDS).

The structural characteristics of the samples grown on the SS310 stainless steel substrates were studied by Raman spectroscopy using a HR800 microscope (LabRam) (HORIBA France SAS, Palaiseau, France) with a 532 nm solid-state laser (0.5 mW, and approximately 1 $\mu m^2$ spot area of the focussed laser beam). To parameterize the main Raman shift peaks of the carbon nanostructures, the range of spectra chosen was from 500 $cm^{-1}$ to 3100 $cm^{-1}$. The positions of the peaks, their full width at half maximum (FWHM) and the relationships between the intensities of the main Raman peaks were analysed from the three spectra acquired from different positions of each sample. From this analysis, the changes of the structural characteristics of carbon nanostructures as a function of the growth temperature were determined. These results were contrasted with the results obtained from the TEM and FE-SEM micrographic images.

## 3. Results and discussion

To determine the effect of growth temperature on carbon nanostructures (ns-C) and its origin, in this section we will relate the results obtained by Raman spectroscopy at different growth temperatures with the observations made by electron microscopy. To do this, we grew a series of carbon nanostructures on SS310 substrates under constant experimental conditions except for the growth temperature. The conditions of the experimental processes are listed in Table 1.

The obtained results allow us to determine the effects of the growth temperature on the structure and morphology of the carbon nanostructures in the explored temperature range (575 to 900 °C).

The growth temperature corresponds to that of the middle zone of the tube furnace, where the substrate was positioned. The oven was heated with a ramp of 1 °C/s and the growth process was started following the stabilization of the temperature of the substrate. The distance between the substrate and the output of the inductively coupled plasma (ICP-CVD) antenna was kept at 40 cm for all samples.

The growth conditions of the carbon nanostructures correspond to a remote plasma, where the radicals (H, $H_2$, and $C_nH_m$) that reach the sample depend on the lifetime of each species. The flow and pressure of the gas are primary parameters that allow modulating the arrival of different species to the growing sample. The speed of the gas ($CH_4$ and radicals) that grazes the substrate was kept constant in all the experiments.

Capacitively-coupled plasma (CCP) favours the growth of carbon nanotubes (CNT) from catalyst seeds of Fe nanoparticles [30]. In contrast, inductively-coupled plasma (ICP) favours the growth of vertical graphene nanowalls, which do not need catalyst to grow [31,32]. At a pressure of 100 Pa, the typical electron density ($n_e$) is around $10^{12}$ $cm^{-3}$ for inductively-coupled neutral plasmas, one order of magnitude higher than capacitively coupled plasmas [31], because the fractional ionization rate of the inductively coupled plasma can be up to 100 times higher [33,34]. For ICP-CVD of pure methane at 100 Pa and 700 °C, the ionization coefficient $\chi_i = \frac{n_e}{n_e+n_g} \sim 10^{-4}$, being $n_g$ the methane gas density, and the ion density $n_i \cong n_e$ (electron density) because the quasi-neutrality of the plasma. The collisions between charged particles (electron-electron, electron-ion, and ion-ion) at $\chi_i \sim 10^{-4}$ are unlikely, and the mean-free-path between two reactive collisions of electron/ion is $\lambda_i = \frac{1}{n_e \sigma_j} \gtrsim 0.5$ m (being $\sigma_j$ the $j$ charged-specie cross section), which is higher than the chamber dimensions. Then, the direct electron-ion recombination is negligible in the volume of the ICP process, working at pressures lower than 100 Pa, and the recombination mainly takes place on the inner surfaces or on the substrate.

In thermal CVD, <0.0002% of the incoming methane dissociates to form active species in the gas phase. However, in plasma-CVD, dissociation is due to frequent electron/$CH_4$ collisions, and >90% of the ionic species produced are radicals such as $H^+$, $H_2^+$, $CH^+$, and $C_2H_2^+$ [35], which give rise to other reactive species and radicals by dissociation and reactive association. In the tubular configuration of the ICP-CVD reactor that we have used in the present study, radicals and neutral ions are generated remotely in the ICP resonator, where the confined electrons have a high density. The radicals produced in the collisions with electrons are carried away by the gas flow and are deposited on the inner walls of the quartz tube or on the substrate, after an insignificant number of reactive collisions in the gas phase. Finally, after 2–3 s of residence time in the gas phase, radicals such as $CH_x$ and $C_2$, which are the most important species in $CH_4$ discharges [36] for the growth of carbon nanostructures, are deposited on the substrate located 40 cm from the dissociation/ionization zone.

### 3.1. Plasma gas composition by optical emission spectroscopy

Fig. 1a shows the OES spectra of the remote plasma, using pure $CH_4$ at the conditions of Tables 1 and 650 °C, after 20 min of deposition. We note that atomic (656 nm, $H_\alpha$) and molecular (550–640 nm, $H_2$) hydrogen recombination lines dominate in the emission spectrum, and originate from the gas precursor $CH_4$ (1:4). Hydrogen atoms are formed as a result of $CH_4$ dissociation in a high-density plasma and provide efficient removal of amorphous carbon (by etching). The etched $CH_x$ radicals can contribute to the growth of VGNWs together with the dissociated ones, since pure hydrocarbon radicals can simultaneously

**Table 1**
Main technological parameters for producing the ns-C/SS310 samples by ICP-CVD.

| Substrate | Tilt (°) | Gas | Mass flow rate (sccm) | Pressure (pa) | Growth temperature (°C) | Temperature ramp (°C/s) | RF power (W) | Time (s) |
|---|---|---|---|---|---|---|---|---|
| SS310 | 5 | $CH_4$ | 13 ± 1 | 53.3 ± 0.5 | 575 to 900 | 1.0 ± 0.5 | 400 ± 4 | 1800 |

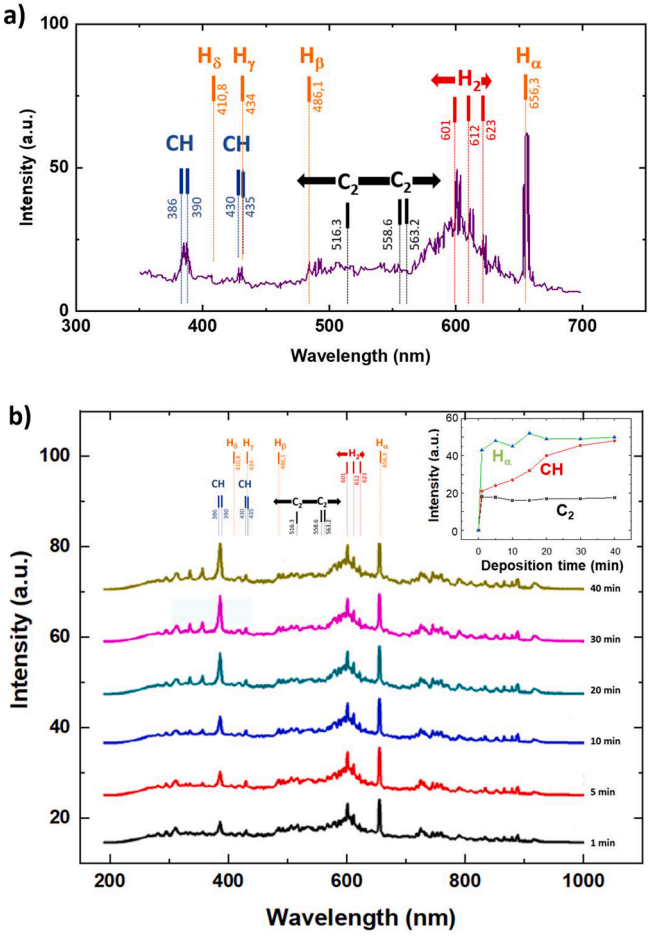


**Fig. 1.** Optical emission spectra obtained during the plasma process of growth of VGNWs by ICP-CVD and 650 °C using pure $CH_4$. a) Bands of emission of CH and $C_2$ radicals, and monoatomic and molecular hydrogen. b) Optical emission spectra of pure $CH_4$ plasma at different deposition times. The top-right representation shows the dependences with deposition time of $H_\alpha$ (green triangle), $C_2$ (black square) and CH (red circle) radicals. (For interpretation of the references to colour in this figure legend, the reader is referred to the web version of this article.)

serve as a carbon source or as a by-product after etching with hydrogen.

The emission lines of the CH radicals at 388 nm and 432 nm, the $C_2$ Swan band system in the range 465–590 nm, and the Balmer lines at 410 nm, 434 nm, 486 nm and 656 nm were analysed. Inside the plasma resonator, the $CH_4$ precursor can be easily converted to $CH_x$ radicals ($x$ = 1–3), to produce $H_yC{=}CH_z$ ($y$, $z$ = 0–2) species and carbon dimers ($C_2$) through recombination of radicals and subsequent dissociation [7].

Fig. 1b shows the optical emission spectra of pure $CH_4$ plasma at different growth times from 0 to 40 min and 650 °C. The inset plot of Fig. 1b shows the concentration evolutions of monoatomic hydrogen ($H_\alpha$ line at 656.3 nm), $C_2$ dimers (Swan band, approximately between 480 and 590 nm), and CH radicals (Table 2) during the 40 min of discharge. The concentration of CH radicals intensifies sharply during the first 20 min of discharge. During this period instabilities of concentration of hydrogen appears. Then, the concentration of CH continues to increase slowly, while hydrogen's remains practically constant.

**Table 2**
OES lines from a pure methane remote plasma excited by ICP-CVD. The deposition parameters are listed in Table 1.

| Wavelength (nm) | Species | Description and effects |
|---|---|---|
| 387<br>430 | CH<br>CH | Emission lines of $CH_x$ radicals ($x$ = 1–3) that are easily formed in the dissociation of the $CH_4$ precursor within the plasma [35]. |
| 465–590 | $C_2$ | Swan band corresponds to carbon dimers ($C_2$) that can be formed through the $CH_x$ radical recombination and subsequent dissociation [7] after 5 min of plasma process (Fig. 1). $C_2$ has a great influence on the nucleation process in the early growth stage [37]. |
| 410, 434, 486, 656 | $H_\delta$, $H_\gamma$, $H_\beta$, $H_\alpha$ | Balmer series from electronic transitions of atomic hydrogen. Atomic hydrogen preferentially etches the amorphous phase of carbon and can induce crystallization [38]. |
| 550–645 | $H_2$ | Fulcher molecular hydrogen band. $H_2$ etches loosely bonded carbon atoms and promotes graphitization into diamond-like carbon [39]. |

The OES spectrum after 5 min of deposition of Fig. 1b, shows a Swan band with a considerable intensity, which after a strong increase decreases slightly until 10 min due to nucleation. As reported, species' density based on $C_2H_x$ ($x$ = 4–6) takes values between $10^{15}$ and $10^{17}$ $m^{-3}$ [35], depending on plasma conditions. In our experimental conditions, the species based on >C=C < are present but have a lower density. These precursor species, allow the initial growth of vertical nanostructures without the presence of catalyst, in contrast to, for example, the Fe nanoparticles needed in CNT growing processes. After the initial nucleation, these precursor species facilitate further growth without catalyst from the VGNW edges.

The plasma containing atomic hydrogen (evidenced in ICP-CVD by the $H_\alpha$ emission line of Fig. 1b) has been shown to be effective in promoting the crystallinity of carbon materials by the following factors: (1) induces crystallization [38,40] and (2) affects preferentially the amorphous phase and acts as an etchant that quickly removes defects (amorphous carbon). On the former, it promotes, on the one hand, a crystalline graphitized structure at the graphene nanowalls growth edges, and on the other hand, prevents the formation of secondary nuclei, which could interfere with the graphene nanowalls growth.

Cheng et al. reported that the hydrogen radical etched loosely bonded carbon atoms and promoted graphitization into diamond-like carbon (DLC) films [41]. In our case, the hydrogen radical would remove disordered components (carbon atoms) like amorphous carbon instead of ordering them, because the bond strength of disordered carbons is weaker than that of ordered ones. Therefore, the hydrogen radical would selectively remove the disordered phase and thus decrease the formation of disordered carbon, which would positively affect the growth of graphene nanowalls [32].

### 3.2. Effect of growth temperature on the mass deposition rate

In order to estimate the specific surface area, we calculated the mass deposition rate, $R$, defined as the mass of material deposited on the substrate per unit area ($cm^2$) and unit time (s). The mass of material deposited was determined from the difference between the mass (substrate and carbon nanostructures) at the end of growth and the mass of

the substrate before the experiment. A 100 μg precision balance was enough to determine the deposited mass with an uncertainty of 5% for substrates of 20 $cm^2$ and a standard deviation of 25% for samples grown at the same conditions.

Fig. 2 shows the raw results of the deposited mass normalized to the substrate's surface (or the specific surface mass, $M_S$, measured with μg/$cm^2$) of the deposited carbon on SS310 substrate foils as a function of the growth temperature.

The curve presents an inflection at temperatures between 700 °C and 775 °C, which in principle could point to the existence of different carbon structures depending on the growth temperature. To validate this, we have analysed the behaviour of Fig. 2 from the point of view of the mass deposition rate, *R*.

### 3.3. Carbon nanostructures grown on SS310 substrate

Our interpretation of the behaviours shown in Fig. 2 are based on: (i) the evolution of *R* with the growth temperature (Fig. 3), (ii) the micrographs obtained by electron microscopy (FE-SEM images shown in Fig. 4), (iii) the surface analysis by EDS (results shown in Figs. 5, 6, and 7), and (iv) the evidence provided by the Raman shift spectra of samples at different growth temperatures (Fig. 8).

The deposition rate, *R*, calculated from the specific surface mass density of carbon nanostructures, $M_S$, provides information on the growth of carbon nanostructures as a function of temperature. Fig. 3a shows the graph of *R* versus the growth temperature of the carbon nanostructures. The analysis of the growth process involves numerous mechanisms for carbon incorporation. One of them is the absorption of carbon into the SS310 substrates by diffusion. This mechanism is due to the composition of the SS310 substrate (mainly Fe, ~25% Cr, and ~ 20% Ni). Given the solubility of carbon in iron [42], diffusion already appears from the first steps of carbon deposition, in the entire explored temperature range. Another incorporation mechanism that appears in the lower growth temperature range is based on the carbon nucleation over the metal domains present on the surface of the SS310 substrate [29]. A third incorporation mechanism of carbon is the formation of different carbon nanostructures on the substrate growing from pure methane by ICP-CVD [27].

Fig. 3 shows two representations of the mass growth rate, *R*, versus the growth temperature, *T*. Fig. 3a shows the evolutions of *R*(*T*) with respect to growth temperature. Two similar behaviours characterized by exponential growth, corresponding to two temperature ranges, at high and low temperatures, can be identified as thermally activated growth processes, according to an exponential model (Fig. 3b):

$$R = R_0 \bullet e^{-E_{act}/k_B T} \quad (1)$$

Being $R_0$ a constant related to the initial mass deposition rate, $k_B$ the Boltzmann constant, $E_{act}$ the activation energy, and *T* the absolute temperature of growth.

On the other hand, two behaviours (blue and red dots in Fig. 3a) appear associated with different nanostructures (Fig. 4). The fitting of the Arrhenius plot of *R*(*T*) to the exponential model (eq. 1) (Fig. 3b), provides a constant $R_0 = 2.4 \times 10^{-7} \frac{kg}{m^2 \bullet s}$, and two slopes corresponding to the thermal activation energies of $E^{act}_{high\_T} = (0.58 \pm 0.15)$ eV (at the high temperature region) and $E^{act}_{low_T} = (1.09 \pm 0.21)$eV (at the low temperature region). These energies are consistent with two different carbon nanostructures, being $E^{act}_{high\_T} < E^{act}_{low\_T}$. The intermediate zone (between 675 and 750 °C) would correspond to a mixture of two carbon nanostructures and as a consequence, it does not fully comply with the

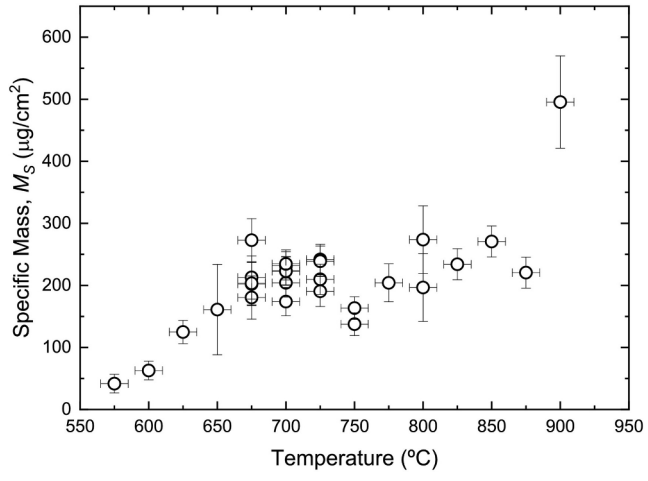


**Fig. 2.** Raw data of specific mass of nanostructured C grown over stainless steel SS310 substrates as a function of the growth temperature. These samples were obtained by ICP-CVD keeping all the technological parameters constant (RF power, methane pressure, mass flow, sample position, and deposition time) except for the growth temperature that was set for each sample in the interval between 575 °C and 900 °C. A considerable number of experiments were carried out in which care was taken to reproduce them with detail in order to reduce dispersion.

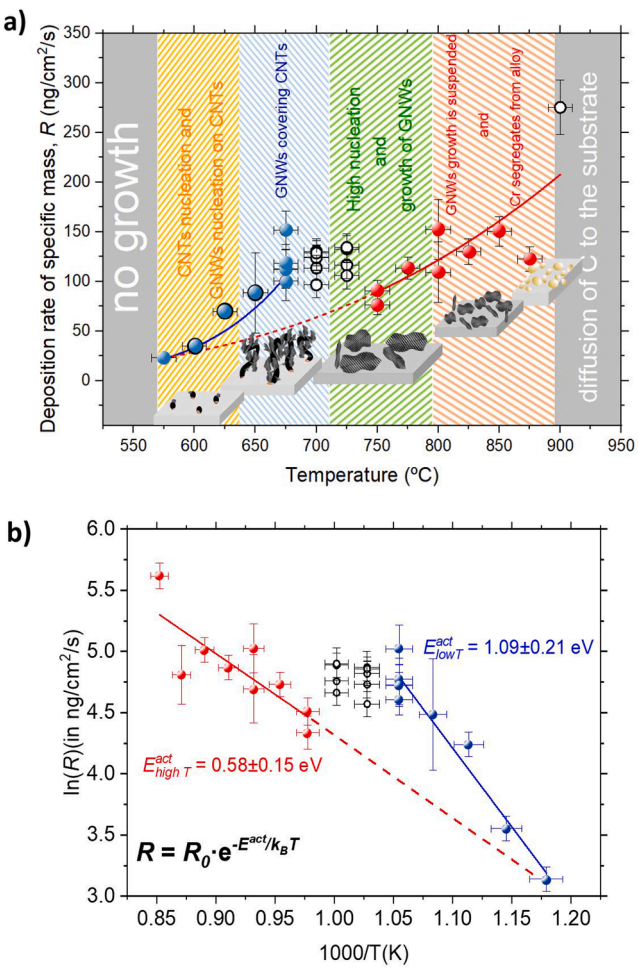


**Fig. 3.** a) Graph of the deposition rate, *R*, determined from the specific surface mass density of carbon nanostructures, $M_S$, and the total time of plasma process (30 min) as a function of the growth temperature of carbon nanostructures on flexible stainless-steel substrates (SS310). b) Arrhenius plot of R, which presents two different slopes corresponding to two respective thermal activation energies. The nanostructures grown at low temperatures between 575 °C and 700 °C have an activation energy $E^{act}_{low_T} = (1.09 \pm 0.21)$eV, while the nanostructures grown at high temperatures (750 °C to 900 °C) have $E^{act}_{high\_T} = (0.58 \pm 0.15)$ eV .

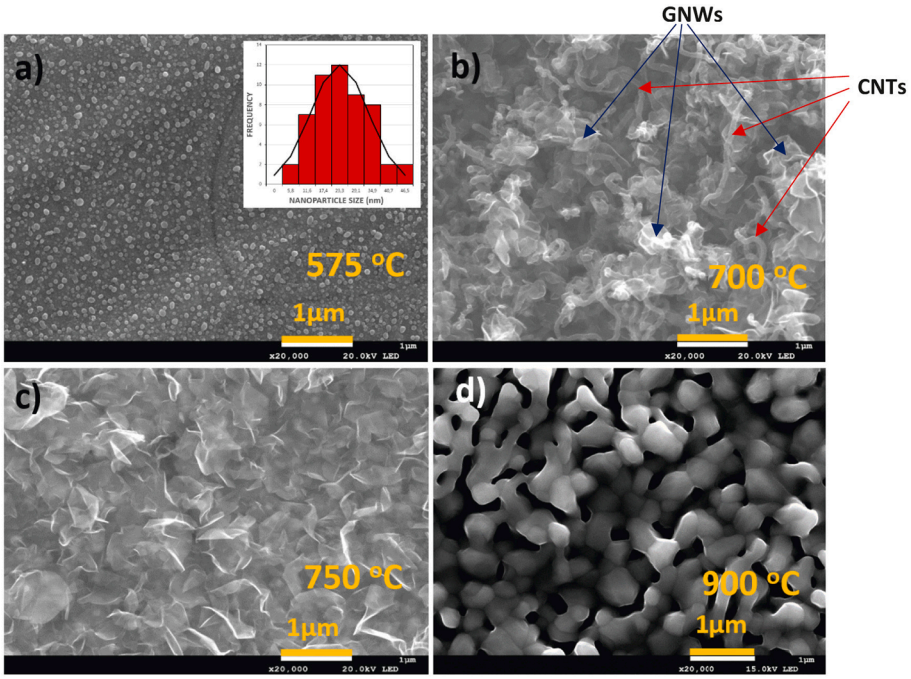


**Fig. 4.** FE-SEM images of carbon nanostructures grown on SS310 substrate by ICP-CVD from $CH_4$, corresponding to different processing temperatures.

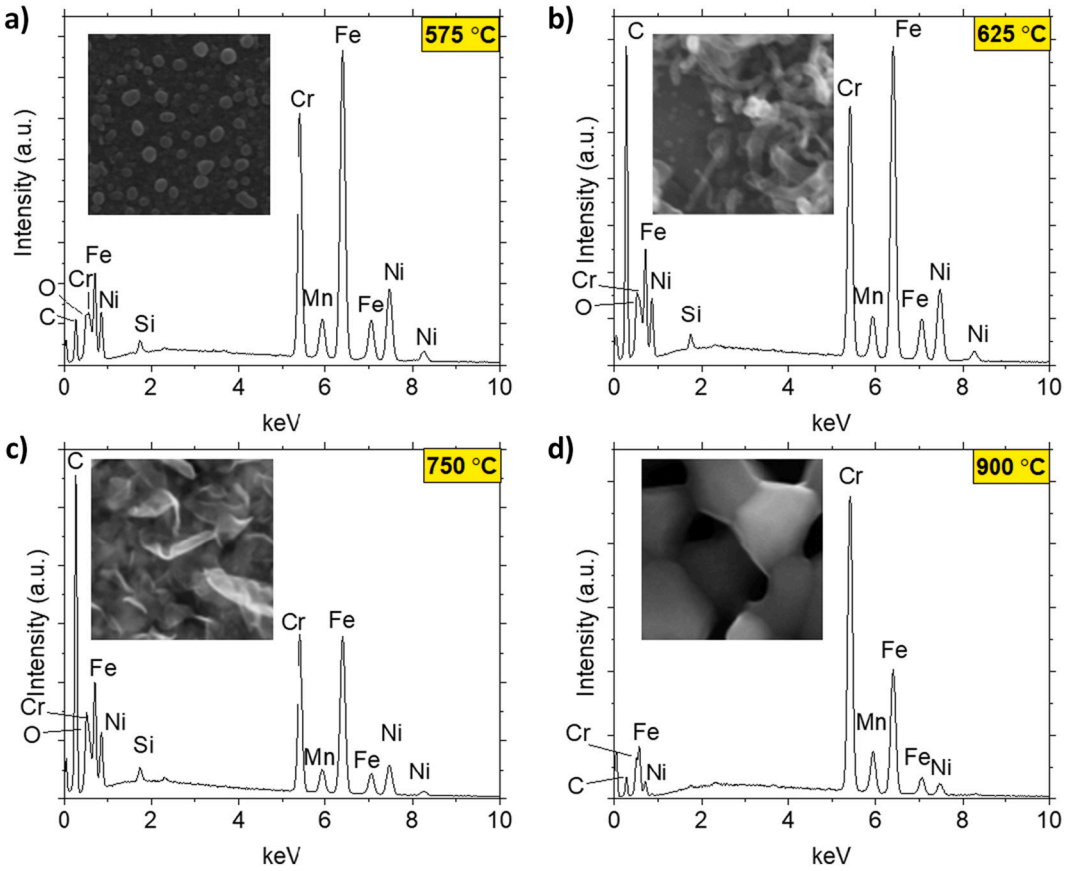


**Fig. 5.** EDS analysis and corresponding SEM images for different growth temperatures (all inset images are 1 µm × 1 µm).

exponential model of eq.1.

Figs. 4a to 4d show the FE-SEM images of carbon-based nanostructures deposited at different temperatures that corroborate the presence of two different nanostructures. The samples were grown at different temperatures while keeping all other technological conditions unaltered.

Fig. 4a shows small nuclei (size 23 ± 10 nm) that correspond to an initial nucleation of carbon on Fe nanodomains located on the surface of

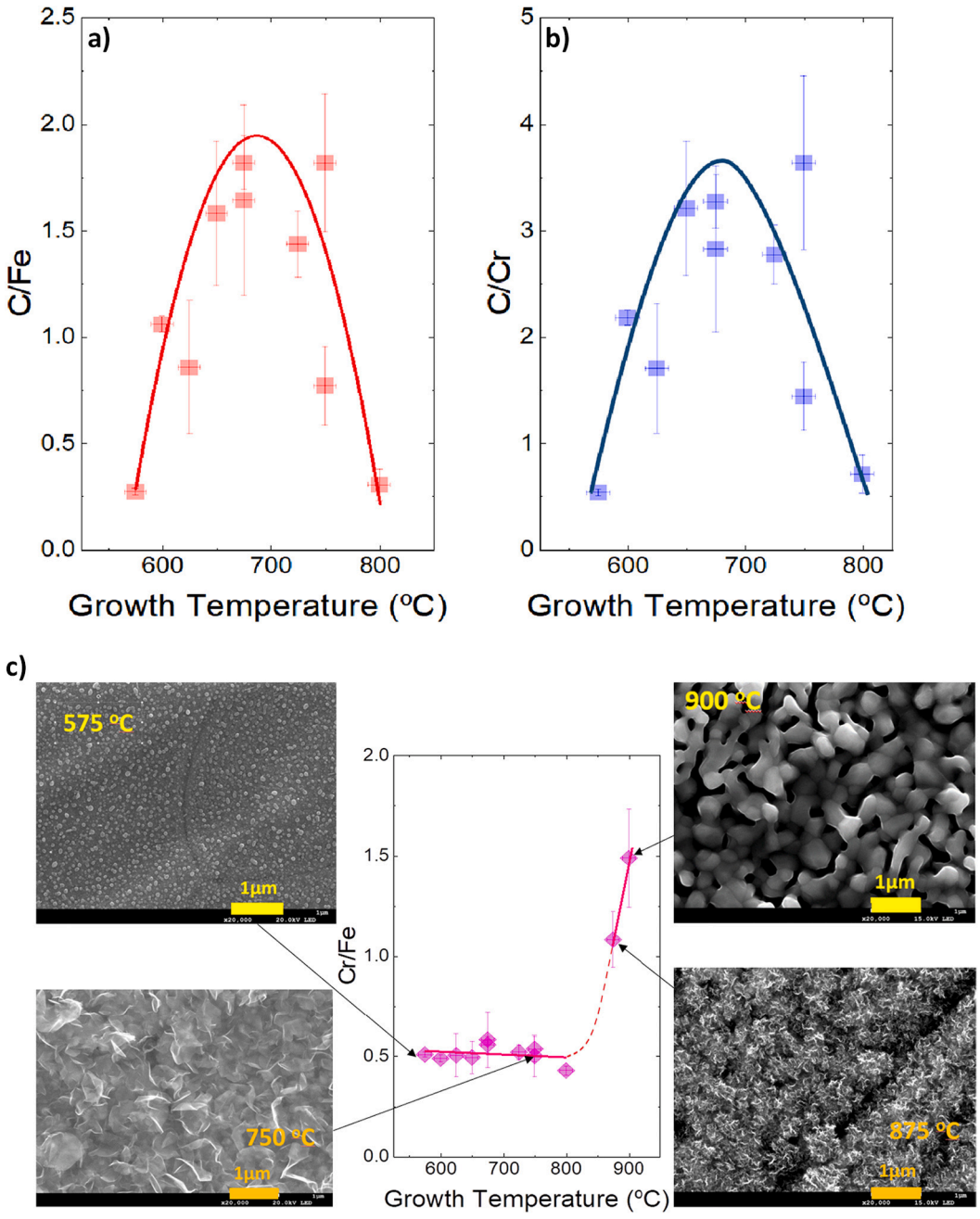


**Fig. 6.** EDS results of the series of samples of GNW grown on SS310 substrate at different temperatures by ICP-CVD.
a) Plot of the carbon/iron concentration ratio that shows a maximum in the temperature range of 650–750 °C. b) Plot of the carbon/chromium density ratio, which also shows a maximum in the same temperature region. c) Graph of the chromium/iron abundance ratio. The highest chromium abundance appears at 900 °C, whereas for temperatures below 800 °C, the Cr/Fe ratio is almost constant and corresponds to the original composition of the SS310 alloy.

the stainless steel substrate at 575 °C [29,43]. In the corresponding EDS spectrum shown in Fig. 5a, the carbon peak near 250 eV is very low, which is consistent with an early stage of carbon nanostructure growth. Carbon nucleation, at medium temperatures, —from 625 °C to 700 °C—, gives rise to the growth of carbon nanotubes, which can be clearly distinguished in Fig. 4b.

The activation energy of the growth of CNTs corresponds to 1.09 ± 0.21 eV from the fitting of Fig. 3b. This activation energy can be attributed to the gas phase decomposition of methane into $CH_x$ species ($x = 1$–3) during the ICP-CVD process, which dissociate at slightly lower energies than usual by the catalytic action of the Fe nanostructures emerging from the surface of the SS310 substrate [44]. Comparing this value with that obtained by other authors, we see that a lower value of (0.86 ± 0.38)eV of the growth activation energy of vertically aligned carbon nanotubes (VACNTs) in the temperature range between 575 °C and 800 °C was reported as being limited by the dissociation of $C_2H_2$ on the Fe catalyst [45]. Chhowalla et al. found 0.56 eV as the activation energy derived from the Arrhenius plot in the low-temperature range (520 °C–700 °C) of VACNTs grown by PECVD from $C_2H_2$ by the catalytic action of Ni nanoparticles [46]. In both cases, the processes were carried out from a $C_2H_2$ plasma, which even without plasma becomes unstable when reaching 400 °C, while methane (gas used in our experiments) totally dissociates when it reaches 1200 °C in thermal processes.

Moreover, the value around 1.1 eV of the activation energy of CNTs

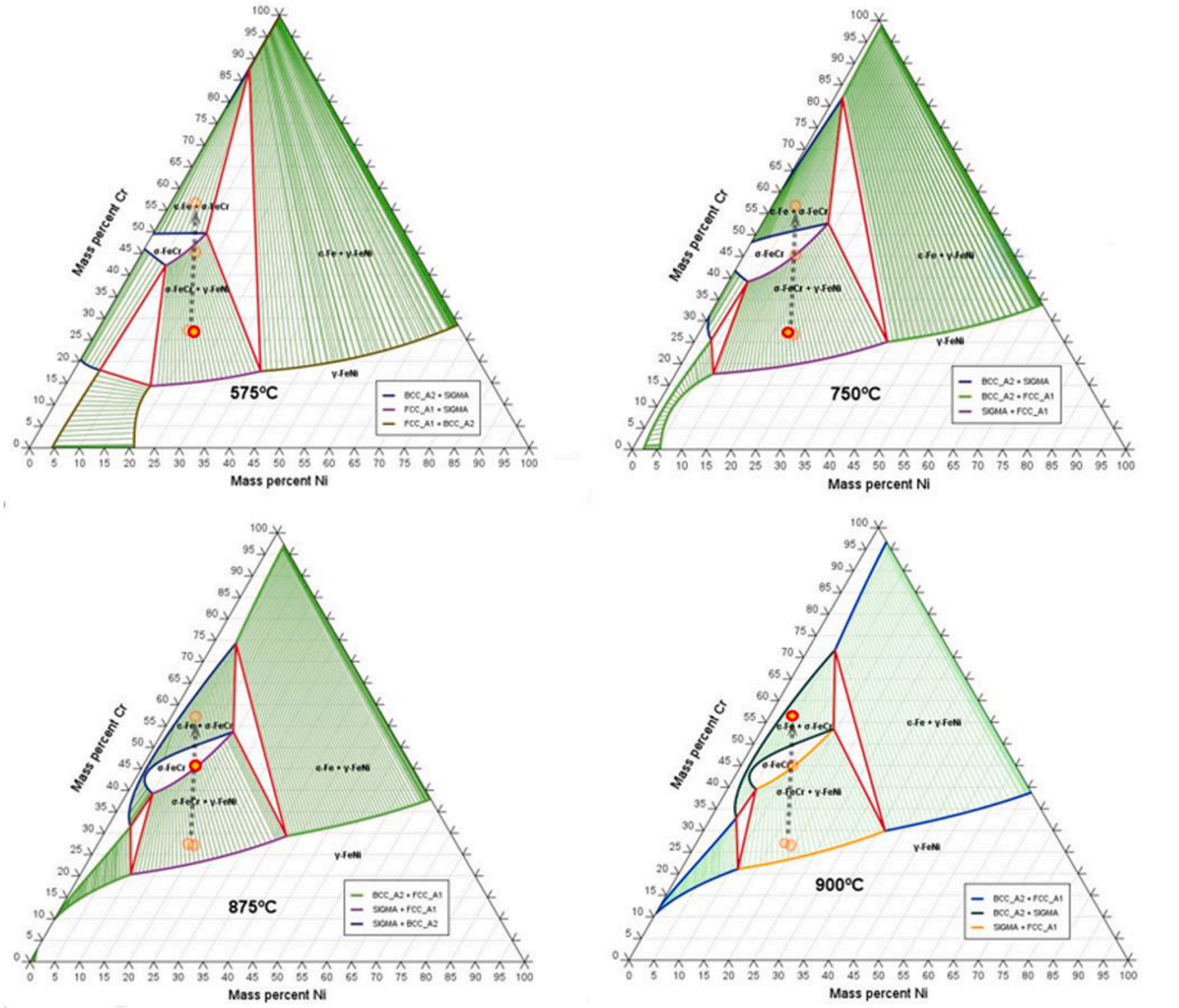


**Fig. 7.** Ternary diagrams of the SS310 substrate at temperatures of 575 °C, 750 °C, 875 °C and 900 °C, where the evolution with temperature of the different phases of the Fe-Cr-Ni system can be seen. The points located in the diagram correspond to the surface composition of the substrate determined by EDS for each temperature (Table 3). The position of the most marked colored point of each diagram corresponds to the composition of the surface at the temperature of the growth process. The phases appearing on the surface evolve from those corresponding to stainless steel SS310 (α-FeCr + γ-FeNi), for temperatures below 750 °C, to the α-Fe + σ-FeCr phases, with the absence of Ni phases, for temperatures >800 °C.

growth is lower than the activation energy values reported by Kharlamova [47], where a large number of CNTs growing processes were reviewed. However, in this review, the growth of CNTs under inductively coupled plasma (ICP) conditions, which allows to reduce the activation energy of the growth process, was not considered. The reduction of activation energy by ICP-CVD is due to the two main distinguishing features of ICP processes: 1) the low ionic bombardment to the growing sample characteristic of ICP with a low ion energy, which facilitates the growth of CNTs with structural defects because of deposition of amorphous carbon; and 2) the high plasma density (if compared with the density values of capacitive coupled plasmas, CCP), which increases the supersaturation of reactive precursor carbon species, and consequently, reduces the growth activation energy barrier to values close to 1.1 eV.

At temperatures between 625 °C and 700 °C, besides curly CNTs the growth of VGNWs was also observed (Fig. 4b). Both CNTs and VGNWs nanostructures appear covering completely the substrate surface (Fig. 4b), the carbon EDS peak (Fig. 5b) being significantly higher as compared to the sample obtained at 575 °C substrate temperature (Fig. 5a). Carbon nanotubes grow due to the catalytic effect of the surface iron nanodomains of the substrate on the carbon precursor species that arrive to the substrate [44], and the nucleation of the VGNWs starts the most probably on the plane of substrate or on the curly CNTs.

The morphology of the carbon nanostructures observed in Fig. 4c (750 °C) shows marked differences with respect to the image of Fig. 4b (700 °C). However, the growth process could be attributed to similar mechanisms. At both temperature values, when the reactive carbon species reach the iron nuclei formed on the SS310 substrate, they give rise to the growth of activated CNTs with an energy of 1.1 eV. However, the reduction of the density of active radicals near the substrate leads to a local reduction of supersaturation conditions until the growth of CNTs stops. The growth process is determined by the substrate temperature, VGNWs partially (Fig. 4b) or completely (Fig. 4c) covering the CNTs, at 700 or 750 °C, respectively. The further growth of CNTs appears limited

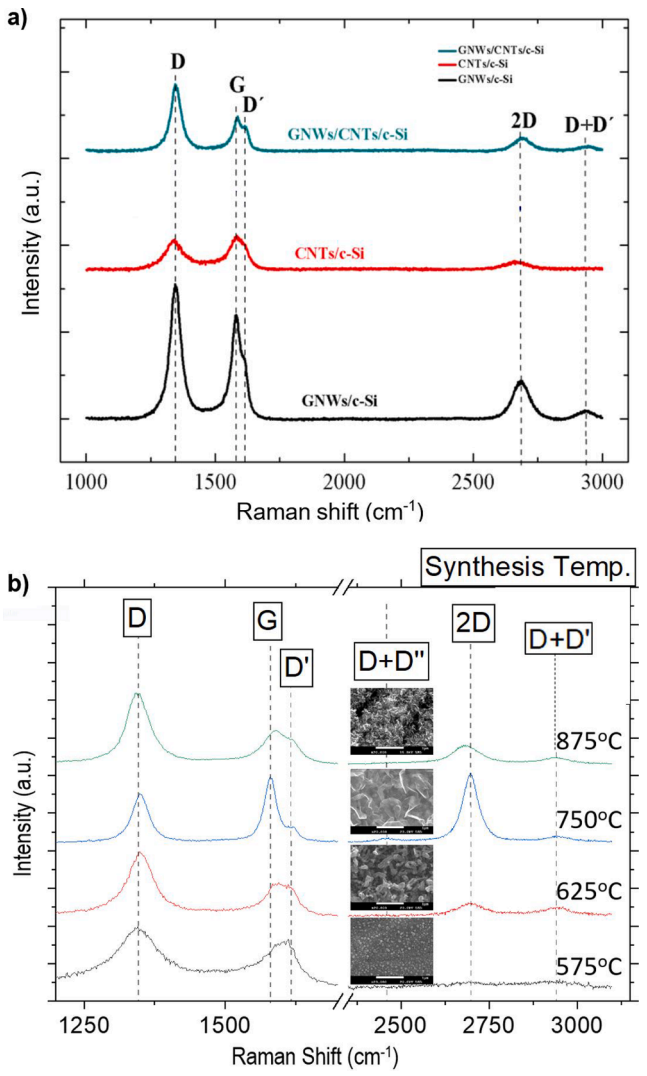


**Fig. 8.** a) Raman spectra of graphene nanowalls (GNWs) and carbon nanotubes (CNTs) grown on c-Si.
b) Normalized Raman spectra of carbon nanostructures grown at different temperatures. At temperatures around 750 °C, graphene nanowalls of sizes around 1 μm present the characteristic 2D peak of graphene and an $I_D/I_G$ ratio lower than 1 indicating a lower number of defects.

by the depletion of reactive carbon radicals near the substrate, which are preferentially deposited on VGNWs in a process with lower activation energy ($E^{act}_{VGNW} = E^{act}_{high\ T} = 0.58$eV) than that of the CNTs ($E^{act}_{CNT} = E^{act}_{low\ T} =$ 1.09eV).

In addition, the VGNWs grown at 700 °C (Fig. 4b) have a smaller size compared to those grown at 750 °C (Fig. 4c), although they maintain the low thickness of very few atomic layers. While at 750 °C the observed nanostructures correspond to VGNWs, like petals of ~1 μm in size and with a thickness of two or more atomic layers, at 700 °C curly-CNTs are clearly observed, while VGNWs are less developed.

Similarly to the sample deposited at 700 °C, the intensity of the EDS carbon peak of the VGNWs grown at 750 °C (Fig. 5c) is very high. Samples grown in the intermediate temperature range of 700 °C–725 °C present a mixture of two different carbon structures, and their behaviour (Fig. 3) does not respond to the exponential model (eq. 1). Fig. 4b evidences the presence of these two carbon nanostructures at the same time. Although the growth process is similar, the CNTs do not appear in the image of Fig. 4c. This is because CNTs only can grow from the stainless steel substrate [29], and as growth proceeds, VGNW nucleate on CNTs and coat them, to the point of blocking diffusion of carbon precursors to the substrate surface, where CNTs grow. At this stage of the process, the CNTs growth rate slows down relative to that of emerging VGNWs.

Strong structural differences in relatively short temperature intervals (25 °C to 50 °C) appear because of the characteristics of the substrate. The high level of chromium (25%) and nickel (21%) of the SS310 alloy, compared to other austenitic steels, results in a lower carbon solubility because this process is limited in the presence of oxygen through the formation of a dense thin coating of chromium oxide. But, under reducing growth conditions due to the presence of hydrogen in our experiments, carburization increases rapidly at temperatures close to 800 °C. At high temperatures, the carburization by the presence of reactive carbon species ($CH_x$) results in diffusion of carbon and subsequent formation of internal carbides close to the surface of the SS310 alloy. At 900 °C the solubility of carbon increases up to three times compared to the solubility at 750 °C. As a consequence, carbon nucleation disappears at 900 °C as carbon diffuses inward forming a zone of internally carburized metal that causes segregation of Cr towards the substrate surface. The evidences of this phenomenology, at process temperatures above 800 °C, is illustrated by Fig. 4d. The strong segregation of Cr at 900 °C is followed by coalescence of Cr-containing particles as evidenced by EDS analysis (Fig. 5d) and collapse the growth of carbon nanostructures.

Consequently, at the highest temperatures (900 °C), the intensity of the carbon EDS peak (Fig. 5d) is short. Now, due to the segregation to the surface of the σ-FeCr phase from the SS310 substrate, a large number of Cr-containing nuclei appears, as evidenced by the images of Figs. 4d and 5d, and the high peak (Cr) in the EDS spectrum near 5.4 keV. These particles are partially sintered, with an average size of 300 nm, and they absorb all the carbon that reaches the substrate, thus limiting the formation of carbon nanostructures [29]. At this point, we should consider that at high temperatures (>875 °C), the Cr phases that emerge from the SS310 substrate, dissolve the carbon species that reach the substrate surface, forming metal carbide phases.

In summary, Figs. 4 and 5 show diverse nanostructures: i) according to the EDS results of Fig. 5a, small nuclei, mainly Fe-based, appear from the Fe nanodomains of the SS310 substrate, which are probably coated with an incipient ultrathin carbon layer (Fig. 4a); ii) a mixture of curly CNTs and VGNWs (Fig. 4b); iii) large VGNWs (Fig. 4c); and iv) sintered microparticles (Fig. 4d), mainly Cr-based, as confirmed by EDS (Fig. 5d), and probably carbon diffused beneath the surface of the SS310 substrate. Their correspondences with the graph in Fig. 3a have been illustrated with schematic drawings in each temperature domain. The EDS results of the surface composition (Fig. 5) point to the presence of carbon in all the samples, although with considerable differences between them as concerns its relative concentrations. While at 575 °C and 900 °C the surface carbon content is quite low, at medium growth temperatures (between 625 °C and 750 °C) the surface carbon content is extreme.

Fig. 6 shows the relative concentrations of elements calculated from the results of EDS surface analysis (corresponding to a depth of 1–3 μm) of the samples obtained at different temperatures. The highest abundance of carbon appears near 700 °C, and for temperatures below 600 °C the growth of carbon nanostructures is almost missed, although nucleation can be seen on the Fe (Fig. 4a). Above 850 °C, a considerable segregation of the Cr phase occurs, which prevents carbon nucleation, leading to diffusion of carbon species into the SS310 substrate. The carbon/iron concentration ratio, [C]/[Fe], (Fig. 6a), and the carbon/chromium concentration ratio, [C]/[Cr], (Fig. 6b) show a maximum in same temperature range of 650–750 °C. The chromium/iron concentration ratio, [Cr]/[Fe], shows a sigmoidal increase with growth temperature. The highest chromium abundance appears at 900 °C. This behaviour at 900 °C is accompanied by an increase in the mass of carbon deposited (Fig. 2), probably due to the increased diffusion of carbon on the very chromium-rich substrate surface. For temperatures below 800 °C, the [Cr]/[Fe] ratio is comparable to the original composition of

the SS310 alloy, [Cr]/[Fe] ~ (25 ± 1) atomic % / (50.5 ± 1.5) atomic %.

The ternary diagrams of the SS310 substrate at temperatures of 575 °C, 750 °C, 875 °C and 900 °C (Fig. 7) show the evolution with temperature of the different phases of the Fe-Cr-Ni system. The points located in the ternary diagrams correspond to the surface composition of the substrate determined by EDS for each substrate temperature value (Table 3). The position of the most contrasting colored point in each diagram corresponds to the composition of the substrate surface at the current growth temperature. As it can be seen in the different diagrams, the phases appearing on the surface of the substrate evolve from those corresponding to stainless steel SS310 (α-FeCr + γ-FeNi), for temperatures below 750 °C, to the α-Fe + σ-FeCr phases, Ni phases being significantly reduced for temperatures >800 °C. This phenomenon, at high temperatures, gives rise to a great dilution of the carbon arriving to the surface of the substrate during the growth process by ICP-CVD, which prevents the growth of carbon nanostructures, carbon species diffusing towards the interior of the substrate, as evidenced in the micrograph corresponding to 900 °C substrate temperature (Fig. 4).

### 3.4. Raman spectroscopy of carbon nanostructures

The structural differences of the carbon nanostructures with the growth temperature were investigated by Raman spectroscopy (Fig. 8). The evolution of the structural characteristics with the growth temperature confirms the structural variations observed by FE-SEM.

Fig. 8a shows the un-normalized Raman spectra of GNWs and CNTs grown on c-Si by ICP-CVD and CCP-CVD, respectively, where the presence of the 2D and D + D′ peaks stand out in the samples containing GNWs [32]. Fig. 8b shows the most characteristic Raman spectra of carbon nanostructures grown at different temperatures in the range between 575 °C and 875 °C. The D band of Raman spectra is associated with the presence of structural defects and edges of the graphene crystal that make possible the breathing mode of the unpacked hexagonal carbon rings [24,48]. The 2D band of Fig. 8b is characteristic of graphenes and a huge enhancement of the 2D mode is clearly observed in the VGNWs grown at temperatures around 750 °C. The 2D band is manifested as a single peak in monolayer graphene, and splits into four clustered peaks in the case of multilayer graphene [48]. So, the full width at half maximum (FWHM) of 2D band of multilayer graphene appears broadened compared to that of the 2D peak of the monolayer graphene.

The presence of the D band along with the G, 2D and D + D′ bands in Fig. 8b points to the growth of two possible carbon nanostructures: graphene nanowalls and carbon nanotubes. Thus, while the 2D band appears for any growth temperature, the D + D′ band, characteristic of GNWs, is very weak or does not appear for the lowest temperatures. This confirms that CNTs are highly disordered and grow at low temperatures, and that around 575 °C there is no growth of GNWs, as seen in the FE-SEM images.

Fig. 8b shows an FE-SEM image corresponding to curled carbon nanotubes (CNT) of diameter 80 ± 10 nm grown at 625 °C from the reduced Fe nanodomains, which appear on the substrate surface after reducing them by a 30 s of $H_2$ plasma excited with 400 W of RF power.

**Table 3**
Surface composition of the SS310 stainless steel alloy substrate determined by EDS, and crystalline phases at different substrate temperatures.

| Substrate temperature (°C) | [Cr] (at. %) | [Fe] (at. %) | [Ni] (at. %) | Phases on substrate surface |
|---|---|---|---|---|
| 575 | 27.0 | 53.4 | 19.6 | α-FeCr + γ-FeNi |
| 625 | 27.0 | 53.7 | 19.3 | α-FeCr + γ-FeNi |
| 675 | 29.8 | 53.5 | 16.7 | α-FeCr + γ-FeNi |
| 750 | 27.3 | 54.6 | 18.1 | α-FeCr + γ-FeNi |
| 800 | 24.5 | 57.3 | 18.2 | α-FeCr + γ-FeNi |
| 875 | 45.9 | 42.5 | 11.6 | σ-FeCr |
| 900 | 56.8 | 38.1 | 5.1 | α-Fe + σ-FeCr |

Also, Fig. 8b shows the Raman spectrum with a high 2D peak and a FE-SEM image corresponding to vertical graphene nanowalls (VGNWs) of few-layer grown at 750 °C, with sizes around 1 μm.

Other minor bands of Fig. 8b are centred at 1616 $cm^{-1}$ (D′, manifested as a right shoulder on the G band and associated with finite-size graphite crystals and graphene edges [49,50]), at 2466 $cm^{-1}$ (D + D″) and at 2949 $cm^{-1}$ (D + D′, originated by two-phonon defect-assisted processes [51,52]).

In order to compare the height of the bands D and G, the stacked spectra of Fig. 8b were normalized to the highest peak of each spectrum. The intensity ratio of D and G bands, $I_D/I_G$, provides information on the number of disordered sites. To quantify the number of defects, we take the profit of the analysis made by Tuinstra and Koenig [53] and the more recent expressions reported by Cançado [51]. According to these works, and assuming a low density of defects regime, we use the equation:

$$L_D^2(nm^2) = (1.8 \pm 0.5) \times 10^{-9} \lambda_L^4 \left(\frac{I_D}{I_G}\right)^{-1} \quad (3)$$

to calculate the distance $L_D$ (in nm) between two point-defects, where $\lambda_L$ is the excitation laser wavelength in nm (532 nm in our case).

Fig. 9a and b show two examples of the fitting of the main Raman peaks (D, G and 2D) of sample grown at 750 °C. In this calculation, the presence of minor peaks such as $G_L$, D′ and D“, as well as the D+D” and D + D′, satellites of peak 2D, have been considered. Fig. 9c and d show the growth temperature dependence of the height ratios of the most characteristic Raman spectra peaks ($I_D$, $I_G$, and $I_{2D}$) of the VGNWs. Fig. 9c shows the dependence of the $I_D/I_G$ ratio on growth temperature, which presents a minimum around 750 °C. As seen in the FE-SEM image of the VGNWs grown at 750 °C (Fig. 8b), the structures have larger areas and a smaller edge-to-surface ratio. Correspondingly, the samples grown in the temperature range between 700 °C and 775 °C present the lowest values of the $I_D/I_G$ ratio (Fig. 9c), which confirms that in this temperature range, there are fewer structural defects.

The evolution of the $I_{2D}/I_G$ ratio shown in Fig. 9d provides information related to the number of graphene layers as a function of growth temperature. The temperature region around 750 °C points to the graphene nanostructures with fewer layers. Our highest value, $I_{2D}/I_G \sim 1.0$ corresponds to VGNW nanostructures grown at 750 °C. Comparing this value with that reported by Gao et al. [54] $I_{2D}/I_G \sim 2.0$, as corresponding to a graphene atomic monolayer, we can conclude that our thinnest VGNWs have more than one atomic layer. Other authors [55] have reported the full width at half maximum (FWHM) of the 2D peak as a direct measure of the number of graphene atomic layers. According with Gao et al., a monolayer corresponds to a value of FWHM (2D peak) between 24 and 31 $cm^{-1}$. Table 4 lists the main Raman spectroscopy peaks corresponding to carbon nanostructures grown over the entire temperature range.

The FWHM values of samples grown in the intermediate temperature range are between 48 $cm^{-1}$ and 65 $cm^{-1}$. These values have been represented as a function of the growth temperature, together with colored bands indicating the number of atomic layers of graphene (Fig. 10a) [55]. The minimum corresponds to two monoatomic-layers for the growth temperature of 700 °C. At 750 °C, FWHM(2D) = 55 ± 2 $cm^{-1}$ that corresponds to graphene nanowalls of two and three monoatomic-layers. Thus, the VGNWs grown at temperatures between 650 °C and 775 °C show thicknesses of 2 to 4 atomic layers (Fig. 10a). This minimum number of atomic layers is probably related to the fact that the nanowalls grown at 700 °C (Fig. 4b) are smaller than the nanostructures grown at 750 °C (Fig. 4c).

Considering the unique morphology of VGNWs, formed by at least two parallel flat vertical monolayers of graphene (scheme of Fig. 10b), it is understood that two is the minimum number of possible atomic layers of VGNW structures.

Fig. 10b shows a schematic representation of the process that prevents the formation of VGNW with less than two monatomic layers. This

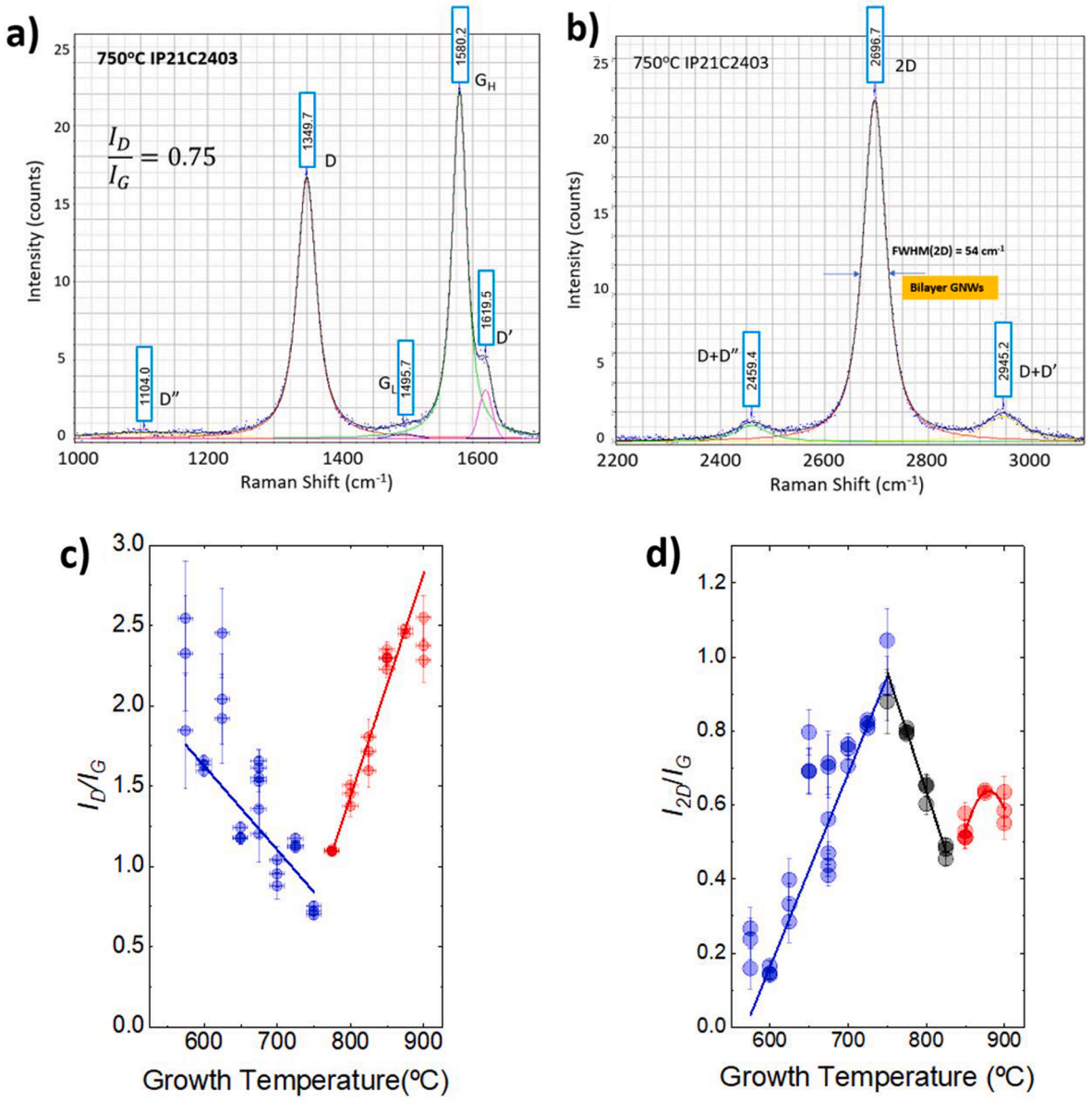


**Fig. 9.** Plots of parameters extracted from the Raman spectra of samples as a function of the growth temperature.
Detail of fitting of the Raman $I_D$ and $I_G$ bands of sample grown at 750 °C.
Detail of fitting of the Raman $I_{2D}$ band of sample grown at 750 °C.
Plot of $I_D/I_G$ ratio versus growth temperature pointing to an opposite evolution of samples grown at lower temperature (blue dots) and those grown at high temperatures (red dots).
Evolution of the $I_{2D}/I_G$ ratio, (For interpretation of the references to colour in this figure legend, the reader is referred to the web version of this article.)

mechanism is due to the fact that the growth of the graphene domains occurs only at their edges, first in the plane of the substrate, and then, upon reaching the coalescence stage without matching the crystalline orientation of the domains, the process of growth continues, forcing the graphene domains to bend. This process gives rise to the formation of graphene nanowalls that protrude from the substrate surface and form 3D nanostructures, in seemingly random directions around the normal direction of the substrate.

For the carbon nanostructures grown on SS310, the inter-defect distance, $L_D$, calculated from $I_D/I_G$ ratio and using eq. 3, with a laser excitation wavelength, $\lambda_L = 532$ nm, is plotted on Fig. 11a as a function of the growth temperature. This dependence shows a maximum at 750 °C, which corresponds to the highest distance between defects, $L_D^{max} = 14.2$ nm.

The temperature range of most interest is between 650 and 800 °C, which corresponds to inter-defect distances $L_D \geq 10$ nm, and to the growth of VGNWs on the substrate. In terms of the defect density, $n_D(cm^{-2}) = 10^{14} \times \frac{2}{\sqrt{3}} L_D^{-2}$, and using eq. 3, we get:

$$n_D(cm^{-2}) = \frac{(6.4 \pm 1.8) \times 10^{22}}{\lambda_L^4} \left(\frac{I_D}{I_G}\right) \quad (4)$$

where, it is shown that the number of defects in the crystal lattice of VGNWs depends linearly on the $I_D/I_G$ ratio. Using eq. 4, valid for the graphene nanostructures grown on SS310, we have calculated the defect densities $n_D$ as a function of growth temperature (Fig. 11b). A minimum appears at the growth temperature of 750 °C, corresponding to the larger VGNWs, with a defect density of $n_D^{750°C} = (5.6 \pm 1.5) \times 10^{11} cm^{-2}$.

The average dimension of the VGNWs grown at 750 °C was estimated through the ImageJ software to be (600 ± 125) nm, hence the average

**Table 4**
Data of main Raman peaks of carbon nanostructures in the range (575 °C -900 °C) of growth temperature.

| T (°C) | D peak ($cm^{-1}$) | | | G peak ($cm^{-1}$) | | | 2D peak ($cm^{-1}$) | | | 2D peak ($cm^{-1}$) | | | $I_D/I_G$ | | | $I_{2D}/I_G$ | | | FWHD 2D ($cm^{-1}$) | # layers |
|---|---|---|---|---|---|---|---|---|---|---|---|---|---|---|---|---|---|---|---|---|
| 575 | 1345.9 | ± | 0.1 | 1592.4 | ± | 5.1 | 2698.0 | ± | 2.7 | 2698.0 | ± | 2.7 | 2.32 | ± | 0.36 | 0.24 | ± | 0.06 | 191.8 | Multilayer |
| 600 | 1343.5 | ± | 0.7 | 1600.3 | ± | 1.0 | 2691.0 | ± | 2.5 | 2691.0 | ± | 2.5 | 1.63 | ± | 0.03 | 0.14 | ± | 0.01 | 195.8 | Multilayer |
| 625 | 1349.5 | ± | 0.7 | 1592.7 | ± | 4.2 | 2696.1 | ± | 0.9 | 2696.1 | ± | 0.9 | 2.04 | ± | 0.28 | 0.33 | ± | 0.06 | 102.5 | Multilayer |
| 650 | 1349.6 | ± | 0.6 | 1581.1 | ± | 0.6 | 2695.0 | ± | 0.2 | 2695.0 | ± | 0.2 | 1.17 | ± | 0.04 | 0.69 | ± | 0.06 | 57.2 | Trilayer |
| 675 | 1348.1 | ± | 2.3 | 1583.8 | ± | 3.0 | 2691.9 | ± | 3.3 | 2691.9 | ± | 3.3 | 1.61 | ± | 0.07 | 0.44 | ± | 0.03 | 83.1 | Multilayer |
| 700 | 1346.5 | ± | 0.9 | 1578.4 | ± | 2.1 | 2694.1 | ± | 3.4 | 2694.1 | ± | 3.4 | 0.95 | ± | 0.08 | 0.75 | ± | 0.03 | 50.1 | Bilayer |
| 725 | 1347.6 | ± | 0.6 | 1580.0 | ± | 0.6 | 2695.4 | ± | 0.4 | 2695.4 | ± | 0.4 | 1.13 | ± | 0.03 | 0.82 | ± | 0.01 | 58.5 | Trilayer |
| 750 | 1350.1 | ± | 0.3 | 1580.4 | ± | 0.3 | 2696.5 | ± | 0.1 | 2696.5 | ± | 0.1 | 0.71 | ± | 0.03 | 0.91 | ± | 0.09 | 54.9 | Bilayer |
| 775 | 1348.4 | ± | 0.5 | 1581.5 | ± | 0.7 | 2696.7 | ± | 0.5 | 2696.7 | ± | 0.5 | 1.09 | ± | 0.00 | 0.80 | ± | 0.01 | 65.0 | Four-layer |
| 800 | 1348.1 | ± | 0.6 | 1583.3 | ± | 0.8 | 2693.1 | ± | 0.7 | 2693.1 | ± | 0.7 | 1.45 | ± | 0.07 | 0.65 | ± | 0.03 | 77.0 | Multilayer |
| 825 | 1348.2 | ± | 0.5 | 1585.6 | ± | 0.1 | 2695.5 | ± | 0.4 | 2695.5 | ± | 0.4 | 1.71 | ± | 0.11 | 0.48 | ± | 0.02 | 85.2 | Multilayer |
| 850 | 1345.8 | ± | 0.2 | 1588.8 | ± | 0.3 | 2686.3 | ± | 0.6 | 2686.3 | ± | 0.6 | 2.29 | ± | 0.05 | 0.52 | ± | 0.03 | 94.1 | Multilayer |
| 875 | 1345.0 | ± | 0.3 | 1588.5 | ± | 0.2 | 2684.1 | ± | 0.8 | 2684.1 | ± | 0.8 | 2.46 | ± | 0.02 | 0.63 | ± | 0.00 | 92.3 | Multilayer |
| 900 | 1344.0 | ± | 0.2 | 1588.2 | ± | 1.1 | 2682.7 | ± | 1.0 | 2682.7 | ± | 1.0 | 2.37 | ± | 0.14 | 0.58 | ± | 0.04 | 97.2 | Multilayer |

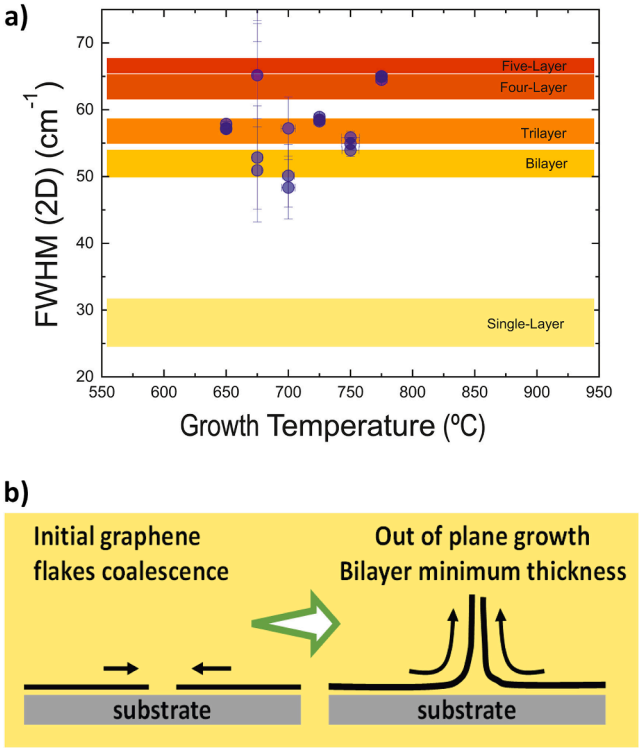


**Fig. 10.** Plot of FWHM of 2D Raman peak versus growth temperature of VGNW's prepared by ICP-CVD.
a) In colored bands there is a correspondence between FWHM (2D) and the number of monoatomic graphene layers.
b) Schematic representation of the process of formation of VGNWs growing from the edges. This process gives rise to the formation of graphene nanowalls that protrude from the surface of the substrate or by nucleation from CNTs, in seemingly random directions around the normal one to the substrate.

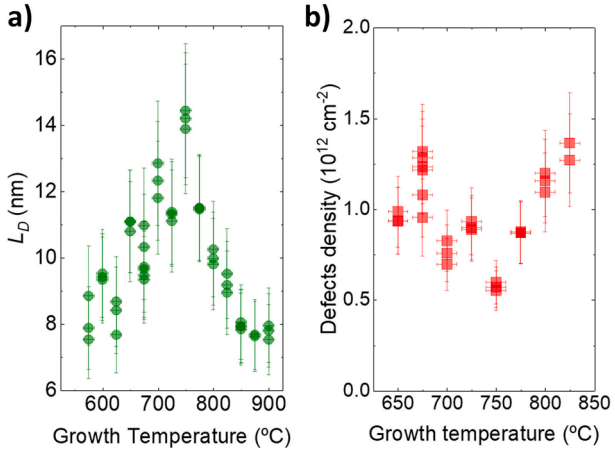


**Fig. 11.** Plots of inter-defect distances and defect densities calculated from the $I_D/I_G$ ratio of the Raman spectra of samples as a function of the growth temperature.
Dependence on growth temperature of the inter-defect distance $L_D$ of the carbon nanostructures calculated from $I_D/I_G$ ratio using eq. 3.
Dependence on growth temperature of the defect density $n_D$ of the graphene nanostructures calculated from $I_D/I_G$ ratio using eq. 4.

number of defects by a nanowall unity (one scale) is around $1.6 \times 10^3$. Considering, from Fig. 4c, an average of 16 VGNW scales/μm$^2$ for samples grown at 750 °C, we can estimate a density of nanowalls on the substrate plane to be $1.6 \times 10^9$ cm$^{-2}$. Then, using eq. 4, the substrate surface density of defects for samples grown at 750 °C is around $2.6 \times 10^{12}$ cm$^{-2}$.

Other interesting parameters for applications to catalysis and energy storage are the specific surface and the total exposed surface by substrate area. In the case of VGNWs grown at 750 °C, and taking into account the estimated number of VGNW scales per substrate area unit (16 VGNW scales/μm$^2$), their average area (0.28 μm$^2$), and VGNWs of two atomic layer of thickness (with two exposed faces), the specific surface is: $S_{spec}$ = 2630 m$^2$g$^{-1}$, which corresponds to the theoretical specific surface of single layer graphene nanowalls (SLG) (one exposed face). The total exposed area of VGNWs has a value nine times higher as compared to the uncovered substrate area. The density of defects determined for VGNWs grown between 650 °C and 825 °C ranges between $2.6 \times 10^{12}$ cm$^{-2}$ and $1.3 \times 10^{12}$ cm$^{-2}$ (relative to the substrate area) (Fig. 11b). These defects are possible places of attachment of metal oxide and metal carbide nanoparticles used in energy storage and catalysis applications [56].

The quality of the graphene nanowalls, as a function of their growth temperature on SS310 stainless steel, has been identified using the results of the Raman spectra from the evolution of the intensity and the FWHM of the G peak with temperature (Fig. 12a). G band corresponds to the $E_{2g}$ phonon [53], and is located around 1581 cm$^{-1}$. FWHM(G) presents a minimum in the temperature range of 650 °C to 750 °C (Fig. 12a), and from the evolution of the intensity of the D peak, $I_D$, located around 1345 cm$^{-1}$. The D peak is due to the breathing modes of sp$^2$ atoms in rings, but requires structural defects for its activation [57,58]. The plot of $I_D/I_G$ versus the growth temperature (Fig. 12b) points to an opposite behaviour of the samples grown at lower

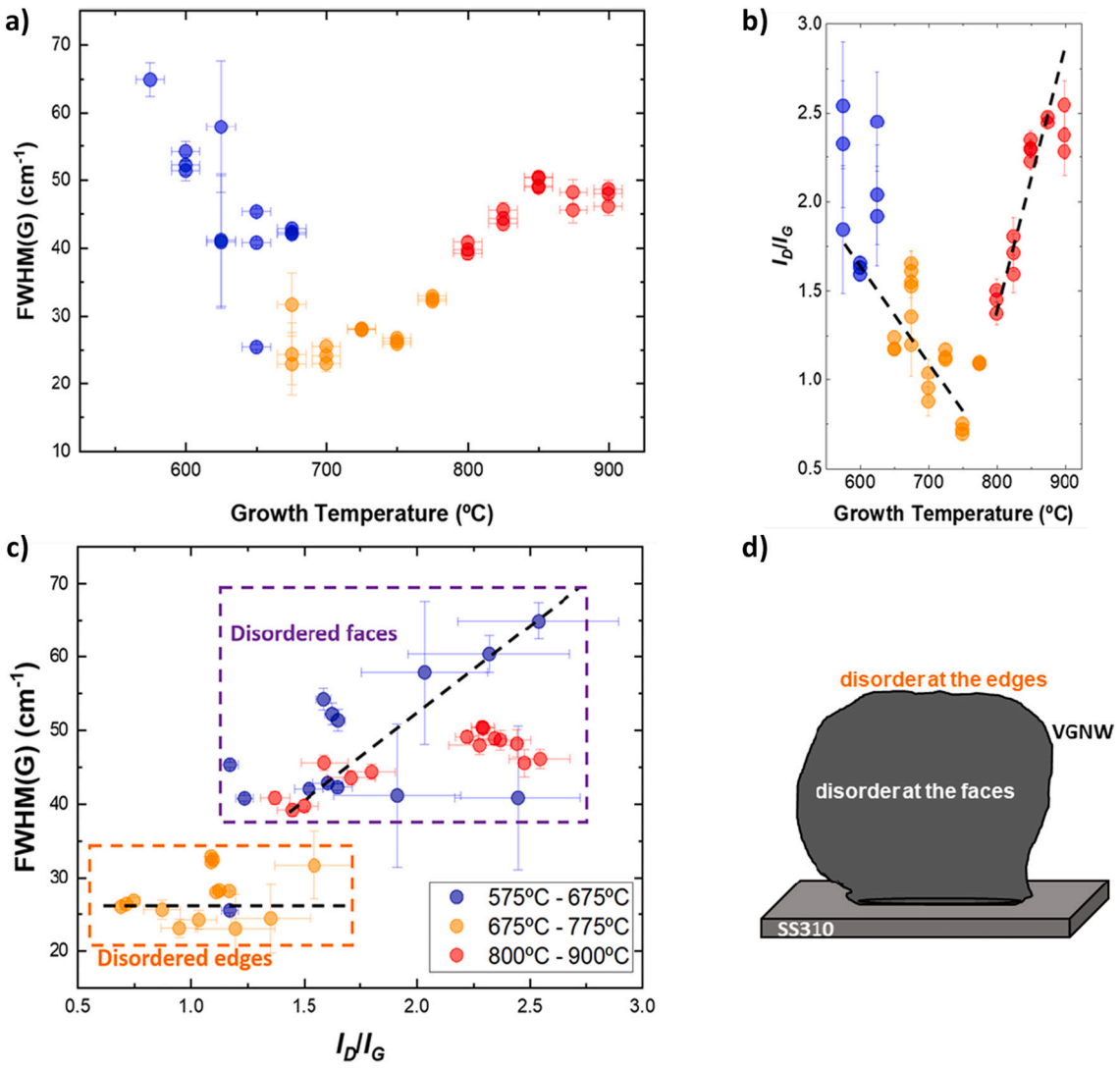


**Fig. 12.** Quality of the graphene nanowalls as a function of the growth temperature on SS310 stainless steel.
a) Evolution of the FWHM of the G peak with growth temperature, with a minimum in the temperature range of 650 °C to 750 °C.
b) Plot of $I_D/I_G$ versus the growth temperature pointing to an opposite behaviour of samples grown at lower temperature (blue and amber points) and the ones grown at high temperatures (red points).
c) Plot representing the FWHM(G) versus the intensity ratio $I_D/I_G$. In the case of disorder located at the edges, FWHM(G) is not correlated with $I_D/I_G$ (flat dashed line) for points inside the bottom-left rectangle, which correspond to the graphene nanowalls having between 2 and 4 atomic layers.
d) Schematic representation of a scale of VGNW grown on SS310 substrate. (For interpretation of the references to colour in this figure legend, the reader is referred to the web version of this article.)

temperature (blue points) and the ones grown at high temperatures (red points). The samples at the deep minimum, grown at temperatures between 650 °C and 775 °C, correspond to a few layers graphene, as confirmed in Fig. 10a.

Typically, in graphene with few monatomic layers, the D peak is associated to nanowall edges rather than defects on nanowall faces [57,59]. Furthermore, in carbon with defects, the FWHM of the G peak, FWHM(G), increases with disorder [51,60]. Combining FWHM(G) with the intensity ratio of the peaks D and G, $I_D/I_G$ (Fig. 12c), allows to discriminate between the disorder located at the edges and the disorder at the faces of the nanowalls of graphene.

This is observed in Fig. 12c, where two regions can be separated: the blue and red points (corresponding to the low and high temperature growth, respectively) showing an increase of FWHM(G) with increasing values of $I_D/I_G$ indicating the presence of disorder mainly at the faces of the nanowalls,—which is consistent with results of eq. 3—, and another region (growth between 675 °C and 775 °C) indicated with amber points where the FWHM(G) does not vary substantially as $I_D/I_G$ rises, corresponding here to disorder located at the edges. This last region where FWHM(G) is not correlated with $I_D/I_G$ (flat dashed line), as shown in the points inside the bottom-left rectangle of Fig. 12c, correspond to the graphene nanowalls having between two and four atomic layers.

## 4. Conclusions

The application of carbon-based nanostructures on electrodes has been widely studied due to their electrical and chemical properties and their large specific surface area, which exceeds values of 2000 $m^2/g$. However, the substrate supporting these nanostructures also plays an important role in certain applications. Thus, the flexible and electrically conductive substrates required in applications such as (i) electrodes for energy storage systems (supercapacitors and batteries) and (ii) catalytic systems, require to be resistant to the chemical environment while relying on abundant and low-priced materials.

The choice of SS310 stainless steel as the support substrate for the carbon nanostructures responds to these requirements, but the relatively high temperature used for the growth of the carbon nanostructures by CVD introduces significant changes in the nanostructures obtained. Temperature-induced structural changes in the stainless steel substrate are also critical in determining the carbon nanostructures' nucleation processes. The two most abundant carbon nanostructures found in the present study grown on SS310 substrates are curly carbon nanotubes (CNTs) and vertically grown graphene nanowalls (VGNWs). The use of the ICP-CVD technique has the advantage of reducing the carbon growth temperature and increasing the growth rate, while maintaining the properties of the substrate when it is kept below 800 °C.

There are several outstanding conclusions in our study. First, the temperature in which graphene nanowalls grow by ICP-CVD on SS310 substrates from pure methane and without catalyst ranges between 675 °C and 775 °C. Second, the characteristics resulting from the analysis with Raman spectroscopy of the graphene nanowalls show that their thickness is at least two monatomic layers, because of the growth mechanism of the graphene nanowalls in 3D formations. Third, the defects in the graphene nanowalls in the temperature range mentioned above reside mainly on the nanowalls' edges—and not on their faces, which affects and facilitates the growth—in a prominent place—of nanoparticles of metallic oxides and carbides for the energy storage and catalysts applications. Fourth, at lower temperatures, below the above temperature range, the growth of curly carbon nanotubes takes place from the iron phase surface nanodomains of the SS310 substrate. Fifth, the growth of these nanotubes is blocked by the formation of graphene nanowalls that prevent the diffusion of the carbon radicals that are precursors of the growth of the CNTs from the insertion in the substrate. Sixth, in electrodes with graphene nanowalls the useful or active surface increases by a factor of 9 with respect to the planar surface of the substrate. And finally, at temperatures above 800 °C, the surface characteristics of the SS310 substrate vary considerably due to the formation of chromium-rich phases on the surface, which largely dissolve and prevent the growth of carbon nanostructures.

## CRediT authorship contribution statement

**Enric Bertran-Serra:** Conceptualization, Methodology, Validation, Formal analysis, Investigation, Resources, Writing – original draft, Writing – review & editing, Visualization, Supervision, Project administration, Funding acquisition. **Arevik Musheghyan-Avetisyan:** Conceptualization, Methodology, Validation, Investigation, Resources, Writing – original draft, Writing – review & editing, Visualization. **Stefanos Chaitoglou:** Conceptualization, Methodology, Validation, Formal analysis, Investigation, Resources, Writing – original draft, Writing – review & editing, Visualization, Funding acquisition. **Roger Amade-Rovira:** Conceptualization, Methodology, Validation, Investigation, Resources, Writing – review & editing, Visualization, Supervision, Project administration, Funding acquisition. **Islam Alshaikh:** Investigation, Resources, Visualization. **Fernando Pantoja-Suárez:** Conceptualization, Validation, Investigation, Writing – original draft, Writing – review & editing, Visualization. **José-Luis Andújar-Bella:** Validation, Investigation, Writing – review & editing. **Tariq Jawhari:** Conceptualization, Methodology, Validation, Formal analysis, Investigation, Writing – original draft, Writing – review & editing. **Angel Perez-del-Pino:** Validation, Investigation, Writing – review & editing, Visualization, Supervision, Project administration, Funding acquisition. **Enikö Gyorgy:** Validation, Investigation, Writing – original draft, Writing – review & editing, Visualization, Supervision, Project administration, Funding acquisition.

## Declaration of Competing Interest

The authors declare that they have no known competing financial interests or personal relationships that could have appeared to influence the work reported in this paper.

## Data availability

Data will be made available on request.

## Acknowledgments

The authors acknowledge financial support from Grant ENE2017-89210-C2-2-R, PID2020-116612RB-C31 and PID2020-116612RB-C32 funded by MCIN/AEI/ 10.13039/501100011033 and, as appropriate, by "ERDF A way of making Europe", by the "European Union" or by the "European Union NextGenerationEU/PRTR". The ENPHOCAMAT group acknowledges support from the *AGAUR* of *Generalitat de Catalunya*, Project No. 2017SGR1086. Two authors (A.M.-A and I.A.) acknowledge the financial supports from APIF grant from *Universitat de Barcelona* and from FPU grant from MEC of Spain. I.A. also acknowledges the support for a 6 months contract, as a research collaborator during the final period of his doctoral thesis, from the project entitled "Textile Competence Centre Vorarlberg 2" (TCCV2) of the program COMET-PROJECTS (Competence Centres for Excellent Technologies) of Austria. Other author (S.C.) acknowledges support from the postdoctoral fellowhips programme *Beatriu de Pinós*, funded by the Secretary of Universities and Research (Government of Catalonia) and by the Horizon 2020 programme of research and innovation of the European Union under the Marie Sklodowska-Curie grant agreement No 801370 (H2020-MSCA-COFUND-2017).

## References

[1] H. Shioyama, Cleavage of graphite to graphene, J. Mater. Sci. Lett. 20 (2001) 499–500, https://doi.org/10.1023/A:1010907928709.
[2] S. Horiuchi, T. Gotou, M. Fujiwara, T. Asaka, T. Yokosawa, Y. Matsui, Single graphene sheet detected in a carbon nanofilm, Appl. Phys. Lett. 84 (2004) 2403–2405, https://doi.org/10.1063/1.1689746.
[3] S. Chaitoglou, E. Bertran, Effect of temperature on graphene grown by chemical vapor deposition, J. Mater. Sci. 52 (2017) 8348–8356, https://doi.org/10.1007/s10853-017-1054-1.
[4] Y. Ando, X. Zhao, M. Ohkohchi, Production of petal-like graphite sheets by hydrogen arc discharge, Carbon. 35 (1997) 153–158, https://doi.org/10.1016/S0008-6223(96)00139-X.
[5] W. Takeuchi, M. Ura, M. Hiramatsu, Y. Tokuda, H. Kano, M. Hori, Electrical conduction control of carbon nanowalls, Appl. Phys. Lett. 92 (2008), 213103, https://doi.org/10.1063/1.2936850.
[6] K. Lehmann, O. Yurchenko, J. Melke, A. Fischer, G. Urban, High electrocatalytic activity of metal-free and non-doped hierarchical carbon nanowalls towards oxygen reduction reaction, Electrochim. Acta 269 (2018) 657–667, https://doi.org/10.1016/j.electacta.2018.03.054.
[7] Z. Bo, Y. Yang, J. Chen, K. Yu, J. Yan, K. Cen, Plasma-enhanced chemical vapor deposition synthesis of vertically oriented graphene nanosheets, Nanoscale. 5 (2013) 5180, https://doi.org/10.1039/c3nr33449j.
[8] N. Shang, P. Papakonstantinou, P. Wang, S. Ravi, P. Silva, Platinum integrated graphene for methanol fuel cells, J. Phys. Chem. C 114 (2010) 15837–15841, https://doi.org/10.1021/jp105470s.
[9] Y. He, W. Chen, X. Li, Z. Zhang, J. Fu, C. Zhao, E. Xie, Freestanding three-dimensional graphene/$MnO_2$ composite networks as ultralight and flexible supercapacitor electrodes, ACS Nano 7 (2013) 174–182, https://doi.org/10.1021/nn304833s.
[10] W. Qiu, H. Xiao, Y. Li, X. Lu, Y. Tong, Nitrogen and phosphorus Codoped vertical graphene/carbon cloth as a binder-free anode for flexible advanced potassium ion full batteries, Small. 1901285 (2019), https://doi.org/10.1002/smll.201901285.
[11] S. Cui, X. Guo, R. Ren, G. Zhou, J. Chen, Decoration of vertical graphene with aerosol nanoparticles for gas sensing, J. Phys. D. Appl. Phys. 48 (2015), 314008, https://doi.org/10.1088/0022-3727/48/31/314008.
[12] K. Chi, X. Zhang, X. Tian, Z. Zhang, Z. Wu, F. Xiao, S. Wang, High-performance flexible asymmetric supercapacitors facilitated by N-doped porous vertical graphene Nanomesh arrays, ChemElectroChem. 7 (2020) 406–413, https://doi.org/10.1002/celc.201901499.
[13] L. Zhu, Y. Huang, Z. Yao, B. Quan, L. Zhang, J. Li, C. Gu, X. Xu, Z. Ren, Enhanced polarization-sensitive terahertz emission from vertically grown graphene by a dynamical photon drag effect, Nanoscale. 9 (2017) 10301–10311, https://doi.org/10.1039/C7NR02227A.
[14] N.G. Shang, F.C.K. Au, X.M. Meng, C.S. Lee, I. Bello, S.T. Lee, Uniform carbon nanoflake films and their field emissions, Chem. Phys. Lett. 358 (2002) 187–191, https://doi.org/10.1016/S0009-2614(02)00430-X.
[15] R. Amade, A. Muyshegyan-Avetisyan, J. Martí González, A.X. Martí Pino, E. György, E. Pascual, J.L. Andújar, E.B. Serra, Super-capacitive performance of

manganese dioxide/graphene Nano-walls electrodes deposited on stainless steel current collectors, Materials. 12 (2019) 483, https://doi.org/10.3390/ma12030483.
[16] Y. Esqueda-Barrón, A. Pérez del Pino, P.G. Lebière, A. Musheghyan-Avetisyan, E. Bertran-Serra, E. György, C. Logofatu, Boost of charge storage performance of graphene Nanowall electrodes by laser-induced crystallization of metal oxide nanostructures, ACS Appl. Mater. Interfaces 13 (2021) 17957–17970, https://doi.org/10.1021/acsami.1c00951.
[17] R. Amade, I. Alshaikh, A. Musheghyan-Avetisyan, E. Bertran-Serra, Enhanced capacitance of manganese oxide driven by hierarchically structured carbon nanotube-carbon nanowall composite, Surf. Coat. Technol. 428 (2021), 127885, https://doi.org/10.1016/j.surfcoat.2021.127885.
[18] S. Chaitoglou, R. Amade, E. Bertran, Evaluation of graphene/WO3 and graphene/CeO x structures as electrodes for supercapacitor applications, Nanoscale Res. Lett. 12 (2017) 635, https://doi.org/10.1186/s11671-017-2385-1.
[19] J. Cao, T. Huang, R. Liu, X. Xi, D. Wu, Nitrogen-doped carbon coated stainless steel meshes for flexible supercapacitors, Electrochim. Acta 230 (2017) 265–270, https://doi.org/10.1016/j.electacta.2017.02.001.
[20] K. Yu, Z. Bo, G. Lu, S. Mao, S. Cui, Y. Zhu, X. Chen, R.S. Ruoff, J. Chen, Growth of carbon nanowalls at atmospheric pressure for one-step gas sensor fabrication, Nanoscale Res. Lett. 6 (2011) 202, https://doi.org/10.1186/1556-276X-6-202.
[21] A. Giese, S. Schipporeit, V. Buck, N. Wöhrl, Synthesis of carbon nanowalls from a single-source metal-organic precursor, Beilstein J. Nanotechnol. 9 (2018) 1895–1905, https://doi.org/10.3762/bjnano.9.181.
[22] A. Malesevic, R. Vitchev, K. Schouteden, A. Volodin, L. Zhang, G.V. Tendeloo, A. Vanhulsel, C.V. Haesendonck, Synthesis of few-layer graphene via microwave plasma-enhanced chemical vapour deposition, Nanotechnology. 19 (2008), 305604, https://doi.org/10.1088/0957-4484/19/30/305604.
[23] M. Hiramatsu, Y. Nihashi, H. Kondo, M. Hori, Nucleation control of carbon Nanowalls using inductively coupled plasma-enhanced chemical vapor deposition, Jpn. J. Appl. Phys. 52 (2013) 01AK05, https://doi.org/10.7567/JJAP.52.01AK05.
[24] S. Hussain, E. Kovacevic, J. Berndt, N.M. Santhosh, C. Pattyn, A. Dias, T. Strunskus, M.-R. Ammar, A. Jagodar, M. Gaillard, C. Boulmer-Leborgne, U. Cvelbar, Low-temperature low-power PECVD synthesis of vertically aligned graphene, Nanotechnology. 31 (2020), 395604, https://doi.org/10.1088/1361-6528/ab9b4a.
[25] H. Wang, X.-B. Li, L. Gao, H.-L. Wu, J. Yang, L. Cai, T.-B. Ma, C.-H. Tung, L.-Z. Wu, G. Yu, Three-dimensional graphene networks with abundant sharp edge sites for efficient Electrocatalytic hydrogen evolution, Angew. Chem. Int. Ed. 57 (2018) 192–197, https://doi.org/10.1002/anie.201709901.
[26] S. Chaitoglou, R. Amade, E. Bertran, Insights into the inherent properties of vertical graphene flakes towards hydrogen evolution reaction, Appl. Surf. Sci. 592 (2022), 153327, https://doi.org/10.1016/j.apsusc.2022.153327.
[27] A. Musheghyan-Avetisyan, F. Güell, P.R. Martínez-Alanis, R. Amade, J. Martí-González, E. Bertran-Serra, Photoluminescence from carbon structures grown by inductively coupled plasma chemical vapor deposition, J. Vac. Sci. Technol. A 38 (2020), 023405, https://doi.org/10.1116/1.5140415.
[28] W. Zheng, X. Zhao, W. Fu, Review of vertical graphene and its applications, ACS Appl. Mater. Interfaces 13 (2021) 9561–9579, https://doi.org/10.1021/acsami.0c19188.
[29] L.F. Pantoja-Suarez, Carbon Nanotubes Grown on Stainless Steel for Supercapacitor Applications, Universitat de Barcelona, 2019. http://hdl.handle.net/2445/142730.
[30] S. Hussain, R. Amade, E. Jover, E. Bertran, Nitrogen plasma functionalization of carbon nanotubes for supercapacitor applications, J. Mater. Sci. 48 (2013) 7620–7628, https://doi.org/10.1007/s10853-013-7579-z.
[31] M. Zhu, J. Wang, R.A. Outlaw, K. Hou, D.M. Manos, B.C. Holloway, Synthesis of carbon nanosheets and carbon nanotubes by radio frequency plasma enhanced chemical vapor deposition, Diam. Relat. Mater. 16 (2007) 196–201, https://doi.org/10.1016/j.diamond.2006.05.007.
[32] A. Musheghyan-Avetisyan, Synthesis and Characterization of Multilayer Graphene Nanostructures, Universitat de Barcelona, 2019. http://hdl.handle.net/2445/142243.
[33] M.A. Lieberman, A.J. Lichtenberg, Principles of Plasma Discharges and Materials Processing: Lieberman/Plasma 2e, John Wiley & Sons, Inc, Hoboken, NJ, USA, 2005, https://doi.org/10.1002/0471724254.
[34] J. Hopwood, C.R. Guarnieri, S.J. Whitehair, J.J. Cuomo, Langmuir probe measurements of a radio frequency induction plasma, J. Vac. Sci. Technol. A 11 (1993) 152–156, https://doi.org/10.1116/1.578282.
[35] S.F. Yoon, K.H. Tan, J. Ahn Rusli, Modeling and analysis of hydrogen–methane plasma in electron cyclotron resonance chemical vapor deposition of diamond-like carbon, J. Appl. Phys. 91 (2002) 40, https://doi.org/10.1063/1.1421038.
[36] S. Kondo, S. Kawai, W. Takeuchi, K. Yamakawa, S. Den, H. Kano, M. Hiramatsu, M. Hori, Initial growth process of carbon nanowalls synthesized by radical injection plasma-enhanced chemical vapor deposition, J. Appl. Phys. 106 (2009), 094302, https://doi.org/10.1063/1.3253734.
[37] N.V. Mantzaris, E. Gogolides, A.G. Boudouvis, A. Rhallabi, G. Turban, Surface and plasma simulation of deposition processes: CH $_4$ plasmas for the growth of diamondlike carbon, J. Appl. Phys. 79 (1996) 3718–3729, https://doi.org/10.1063/1.361205.
[38] S. Vizireanu, S.D. Stoica, C. Luculescu, L.C. Nistor, B. Mitu, G. Dinescu, Plasma techniques for nanostructured carbon materials synthesis. A case study: carbon nanowall growth by low pressure expanding RF plasma, Plasma Sources Sci. Technol. 19 (2010), 034016, https://doi.org/10.1088/0963-0252/19/3/034016.
[39] M. Cheng, B.-W. Wang, P.-X. Hou, J.-C. Li, F. Zhang, J. Luan, H.-T. Cong, C. Liu, H.-M. Cheng, Selective growth of semiconducting single-wall carbon nanotubes using SiC as a catalyst, Carbon. 135 (2018) 195–201, https://doi.org/10.1016/j.carbon.2018.04.047.
[40] M. Zhu, J. Wang, B.C. Holloway, R.A. Outlaw, X. Zhao, K. Hou, V. Shutthanandan, D.M. Manos, A mechanism for carbon nanosheet formation, Carbon. 45 (2007) 2229–2234, https://doi.org/10.1016/j.carbon.2007.06.017.
[41] C.-L. Cheng, C.-F. Chen, W.-C. Shaio, D.-S. Tsai, K.-H. Chen, The CH stretching features on diamonds of different origins, Diam. Relat. Mater. 14 (2005) 1455–1462, https://doi.org/10.1016/j.diamond.2005.03.003.
[42] C.G. Homan, Diffusion of carbon in alpha iron, Acta Metall. 12 (1964) 1071–1079, https://doi.org/10.1016/0001-6160(64)90079-3.
[43] K.C. Sabat, P. Rajput, R.K. Paramguru, B. Bhoi, B.K. Mishra, Reduction of oxide minerals by hydrogen plasma: an overview, Plasma Chem. Plasma Process. 34 (2014) 1–23, https://doi.org/10.1007/s11090-013-9484-2.
[44] I. Chorkendorff, J.W. Niemantsverdriet, Concepts of Modern Catalysis and Kinetics, 1st ed, Wiley, 2003, https://doi.org/10.1002/3527602658.
[45] D.S. Engstrøm, N.L. Rupesinghe, K.B.K. Teo, W.I. Milne, P. Bøgild, Vertically aligned CNT growth on a microfabricated silicon heater with integrated temperature control—determination of the activation energy from a continuous thermal gradient, J. Micromech. Microeng. 21 (2011), 015004, https://doi.org/10.1088/0960-1317/21/1/015004.
[46] M. Chhowalla, K.B.K. Teo, C. Ducati, N.L. Rupesinghe, G.A.J. Amaratunga, A. C. Ferrari, D. Roy, J. Robertson, W.I. Milne, Growth process conditions of vertically aligned carbon nanotubes using plasma enhanced chemical vapor deposition, J. Appl. Phys. 90 (2001) 5308–5317, https://doi.org/10.1063/1.1410322.
[47] M.V. Kharlamova, Investigation of growth dynamics of carbon nanotubes, Beilstein J. Nanotechnol. 8 (2017) 826–856, https://doi.org/10.3762/bjnano.8.85.
[48] T.M.G. Mohiuddin, A. Lombardo, R.R. Nair, A. Bonetti, G. Savini, R. Jalil, N. Bonini, D.M. Basko, C. Galiotis, N. Marzari, K.S. Novoselov, A.K. Geim, A. C. Ferrari, Uniaxial strain in graphene by Raman spectroscopy: G peak splitting, Grüneisen parameters, and sample orientation, Phys. Rev. B 79 (2009), 205433, https://doi.org/10.1103/PhysRevB.79.205433.
[49] A.C. Ferrari, J.C. Meyer, V. Scardaci, C. Casiraghi, M. Lazzeri, F. Mauri, S. Piscanec, D. Jiang, K.S. Novoselov, S. Roth, A.K. Geim, Raman Spectrum of graphene and graphene layers, Phys. Rev. Lett. 97 (2006), 187401, https://doi.org/10.1103/PhysRevLett.97.187401.
[50] S. Kurita, A. Yoshimura, H. Kawamoto, T. Uchida, K. Kojima, M. Tachibana, P. Molina-Morales, H. Nakai, Raman spectra of carbon nanowalls grown by plasma-enhanced chemical vapor deposition, J. Appl. Phys. 97 (2005), 104320, https://doi.org/10.1063/1.1900297.
[51] L.G. Cançado, A. Jorio, E.H.M. Ferreira, F. Stavale, C.A. Achete, R.B. Capaz, M.V. O. Moutinho, A. Lombardo, T.S. Kulmala, A.C. Ferrari, Quantifying defects in graphene via Raman spectroscopy at different excitation energies, Nano Lett. 11 (2011) 3190–3196, https://doi.org/10.1021/nl201432g.
[52] A.C. Ferrari, D.M. Basko, Raman spectroscopy as a versatile tool for studying the properties of graphene, Nature Nanotech. 8 (2013) 235–246, https://doi.org/10.1038/nnano.2013.46.
[53] F. Tuinstra, J.L. Koenig, Raman Spectrum of graphite, J. Chem. Phys. 53 (1970) 1126–1130, https://doi.org/10.1063/1.1674108.
[54] L. Gao, J.R. Guest, N.P. Guisinger, Epitaxial graphene on cu(111), Nano Lett. 10 (2010) 3512–3516, https://doi.org/10.1021/nl1016706.
[55] Y. Hao, Y. Wang, L. Wang, Z. Ni, Z. Wang, R. Wang, C.K. Koo, Z. Shen, J.T. L. Thong, Probing layer number and stacking order of few-layer graphene by Raman spectroscopy, Small. 6 (2010) 195–200, https://doi.org/10.1002/smll.200901173.
[56] S. Chaitoglou, R. Amade, R. Ospina, E. Bertran, Hybrid nanostructured compounds of Mo2C on vertical graphene Nanoflakes for highly efficient hydrogen evolution reaction Electrocatalysis, SSRN J. (2022), https://doi.org/10.2139/ssrn.4151703.
[57] V. Bianchi, T. Carey, L. Viti, L. Li, E.H. Linfield, A.G. Davies, A. Tredicucci, D. Yoon, P.G. Karagiannidis, L. Lombardi, F. Tomarchio, A.C. Ferrari, F. Torrisi, M. S. Vitiello, Terahertz saturable absorbers from liquid phase exfoliation of graphite, Nat. Commun. 8 (2017) 15763, https://doi.org/10.1038/ncomms15763.
[58] A.C. Ferrari, J. Robertson, Interpretation of Raman spectra of disordered and amorphous carbon, Phys. Rev. B 61 (2000) 14095–14107, https://doi.org/10.1103/PhysRevB.61.14095.
[59] C. Casiraghi, A. Hartschuh, H. Qian, S. Piscanec, C. Georgi, A. Fasoli, K. S. Novoselov, D.M. Basko, A.C. Ferrari, Raman spectroscopy of graphene edges, Nano Lett. 9 (2009) 1433–1441, https://doi.org/10.1021/nl8032697.
[60] A.C. Ferrari, S.E. Rodil, J. Robertson, Interpretation of infrared and Raman spectra of amorphous carbon nitrides, Phys. Rev. B 67 (2003), 155306, https://doi.org/10.1103/PhysRevB.67.155306.